Agricultural and Forest Meteorology 362 (2025) 110342

Contents lists available at ScienceDirect

Agricultural and Forest Meteorology

journal homepage: www.elsevier.com/locate/agrformet

On the application of the hockey-stick transition hypothesis to characterize turbulence within and above a deciduous forest

Temple R. Lee [a,*], Sandip Pal [b], Praveena Krishnan [a], Tim B. Wilson [a,c], Rick D. Saylor [a], Tilden P. Meyers [d], John Kochendorfer [a], Will Pendergrass [a], Randy White [a,c], Mark Heuer [a,c]

[a] NOAA/Air Resources Laboratory, Oak Ridge, TN, USA
[b] Department of Geosciences, Atmospheric Sciences Group, Texas Tech University, Lubbock, TX, USA
[c] Oak Ridge Associated Universities, Oak Ridge, TN, USA
[d] NOAA/Air Resources Laboratory, Boulder, CO, USA

ARTICLE INFO

Keywords:
Turbulence
Hockey stick transition
Monin-Obukhov Similarity Theory
Friction velocity
Stability

ABSTRACT

Turbulence governs many atmospheric processes including mixing, transport, and energy transfer. Consequently, there is a strong need for the examination and validation of existing turbulence theories. The HOckey-Stick Transition (HOST) hypothesis was proposed to challenge traditional understanding of near-surface turbulence processes derived from Monin-Obukhov Similarity Theory (MOST). Within the MOST framework, the momentum flux entirely depends upon $\partial\overline{U}/\partial z$ (i.e., the change in mean wind speed ($\overline{U}$) with height (z)), but this relationship is not as straightforward under HOST. Because HOST was developed using observations over relatively uniform, homogeneous terrain, questions arise regarding HOST's applicability within and above heterogeneous forest canopies where multi-level turbulence measurements are somewhat rare but are essential for developing a unified similarity scaling applicable over complex surfaces. To this end, we used one year (1 January 2016 through 31 December 2016) of turbulence measurements sampled at eight heights along a 60-m tower within and above a mixed deciduous forest at Chestnut Ridge in eastern Tennessee in the southeastern U.S. We examined the diurnal and seasonal variability of selected turbulence parameters (i.e., friction velocity (u_*) and turbulence velocity scale (V_{TKE})) to detail the micrometeorological characteristics of the site during the study period. We then used these turbulence measurements to evaluate HOST by determining their relationship with $\overline{U}$ and to assess the dependencies of this relationship on time of day, season, wind direction, and atmospheric stability. We found that HOST is most applicable under very stable regimes, whereas the relationships between u_* and $\overline{U}$, and between V_{TKE} and $\overline{U}$, were more linear above the forest canopy than within the forest canopy and when the canopy was not foliated. Overall, this work builds upon previous studies that have described limitations in MOST and identifies scenarios when the HOST hypothesis may be more applicable than MOST for representing near-surface turbulence processes.

1. Introduction

Describing and predicting the exchanges of energy, mass, and momentum within and above forest canopies remains a challenging task for numerical weather prediction (NWP) models. Consequently, atmospheric boundary layer (ABL) interactions with canopies control multiple processes including, for example, mechanical diffusion, horizontal transport, vertical mixing, and changes in particle eddy diffusivity (Brunet, 2020). Cumulatively, it is well known that the parameterizations based on assumptions for horizontally homogeneous and flat terrain have difficulties simulating surface and ABL processes over complex terrain and complex land cover types (e.g., Wulfmeyer et al., 2011; Fernando et al., 2015). One of the most widely used approaches for representing surface-layer (SL) processes is Monin-Obukhov Similarity Theory (MOST) (Monin and Obukhov, 1954), even though its limitations have been well-documented (e.g., Businger et al., 1971; Andreas and Hicks, 2002; Salesky and Chamecki, 2012; Sun et al., 2020). MOST's limitations include errors in the stability variable employed (i.e., stability parameter, z/L, where L is the Obukhov length scale, and z is the height of interest (Salesky and Chamecki, 2012));

* Corresponding author.
E-mail address: temple.lee@noaa.gov (T.R. Lee).

https://doi.org/10.1016/j.agrformet.2024.110342
Received 1 July 2024; Received in revised form 8 October 2024; Accepted 26 November 2024
Available online 19 December 2024

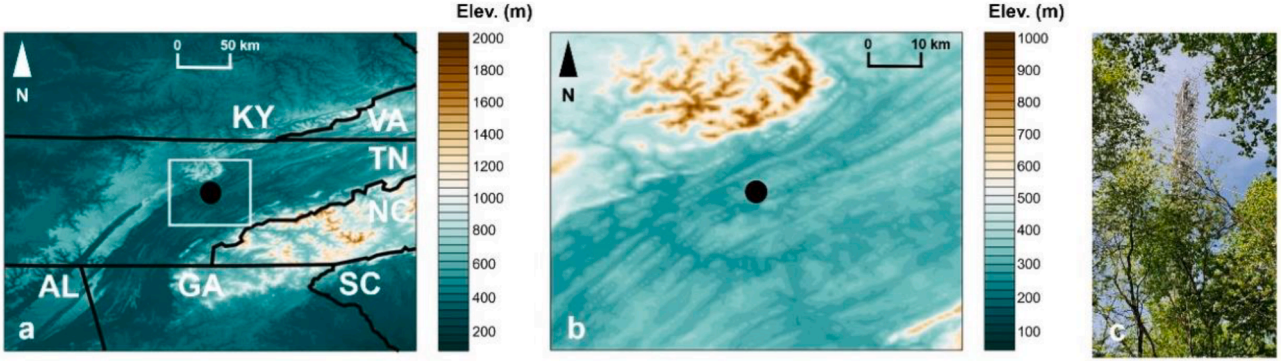

Fig. 1. (a) Location of Chestnut Ridge (black circle) in eastern Tennessee and relative to other states in the Southeast U.S. The box in (a) indicates the location of the map shown in (b). The black circle in panel (b) indicates the location of the Chestnut Ridge tower, pictured in (c) during the growing season. Note the elevation is contoured every 50 m and 25 m in panel (a) and (b), respectively, to highlight the fine-scale elevation variability near the tower. These topography data were obtained from the Parameter-elevation Regressions on Independent Slopes Model (PRISM) climate group.

self-correlation (e.g., Hicks, 1978; Hicks, 1981; Andreas and Hicks, 2002); MOST's performance over mountainous terrain (e.g., Sfyri et al., 2018), within the nocturnal boundary layer (NBL; e.g., Mahrt, 1998; Optis et al., 2014) and, consistent with other conventional paradigms (e.g., Ansorge and Mellado, 2016), within highly-stable atmospheric regimes (e.g., Ansorge and Mellado, 2014; Allouche et al., 2022). These deficiencies have motivated the exploration of alternatives to MOST (e.g., Foken, 2006; Wilson, 2008; Sun et al., 2012; Pal et al., 2013; Lee and Buban, 2020; Lee et al., 2021; Lee and Meyers, 2023; Lee et al., 2023a). One alternative is the HOckey-Stick Transition (HOST) hypothesis, which has been proposed over the past 10–15 years to explain near-surface turbulence regimes (Sun et al., 2012; Van de Wiel et al., 2012; Sun et al., 2015; Sun et al., 2016; Sun et al., 2020; Grisogono et al., 2020; Bhimireddy et al., 2024). HOST challenges classical understanding of turbulence derived from MOST. Under neutral regimes in MOST, the momentum flux entirely depends on $\partial\overline{U}/\partial z$ (i.e., the change in mean wind speed ($\overline{U}$) with height (z)) which is mainly driven by friction velocity as suggested by the Businger-Dyer relationship (Stull, 1988). As noted by Sun et al. (2020), the HOST hypothesis states that the most energetic coherent turbulence eddies near the surface are large and non-local, and energy conservation governs turbulence intensity. Thus, within the HOST framework, there exists little dependence of turbulence parameters, i.e., friction velocity (u_*), vertical velocity variance (σ_w^2), turbulent kinetic energy (*TKE*), turbulence velocity scale (V_{TKE}, which is the square root of *TKE*), on the mean wind speed when wind speeds are low. Instead, turbulence is generated solely by local instabilities within low wind speed regimes (e.g., Bhimireddy et al., 2022). Above a certain wind speed threshold, HOST describes turbulence as being generated by the bulk shear, with an approximately linear relationship between turbulence intensity and wind speed which is consistent with MOST (e.g., Sun et al., 2020). Because of these two unique turbulence regimes, the relationship between turbulence intensity and wind speed is shaped like a hockey stick (e.g., Sun et al., 2012; Sun et al., 2015; Sun et al., 2016; Sun et al., 2020; Yus-Díez et al., 2019; Grisogono et al., 2020).

Like many theories that form the groundwork for SL similarity formulations in boundary-layer meteorology, HOST was developed using measurements obtained from relatively flat terrain, namely from the Cooperative Atmosphere–Surface Exchange Study-1999 (CASES-99) that was conducted in Kansas in 1999 (Poulos et al., 2002). Consequently, there is a strong need to evaluate the applicability of HOST over inhomogeneous land surfaces, for example regions with complex terrain (e.g., Yus-Díez et al., 2019), forest canopies, or areas with fine-scale variations in land cover or land use. To this end, past work evaluating HOST over different land cover types has so far found that the theory is generally applicable to areas with gently-sloping terrain (e.g., Bhimireddy et al., 2022), urban areas (e.g., Liang et al., 2018), polar regions (e.g., Vignon et al., 2017; Chechin, 2021), ocean surfaces (e.g., Andreas et al., 2012), boreal pine forests (e.g., Peltola et al., 2021), and mountainous terrain (e.g., Acevedo et al., 2016; Russell et al., 2016).

Adopting a framework that overcomes MOST's limitations will improve the SL parameterizations used within operational NWP models and in turn help produce better NWP models. Doing so, however, requires that MOST alternatives, including HOST, are rigorously evaluated over a full suite of land cover and land use types, variable stability regimes (i.e., ranging from very stable regimes conditions with $L \gg 0$ to strongly-convective conditions yielding $L \ll 0$), and climatic types (e.g., humid, sub-humid, and arid). Although there has been extensive work evaluating HOST over different land cover types as noted previously (e.g., (Acevedo et al., 2016; Russell et al., 2016; Vignon et al., 2017; Liang et al., 2018)), HOST has not been evaluated within and above forested canopies. Because previous work has indicated that traditional SL parameterizations struggle under weak wind regimes (e.g., Zhang and Zheng, 2004; Lee et al., 2021; Lee and Meyers, 2023), and low wind speeds are prevalent in the Southeast U.S. (e.g., Klink, 1999), this region is uniquely well suited for testing SL parameterizations (e.g., Lee et al., 2021).

In this work, we evaluate the applicability of the HOST hypothesis within and above a forested canopy across different seasons and atmospheric regimes using one year (1 January 2016 through 31 December 2016) of observations of turbulence parameters and meteorological variables obtained from Chestnut Ridge in eastern Tennessee in the Southeast U.S. In Sections 2 and 3, we discuss the measurements from Chestnut Ridge and our data processing techniques, respectively. In Section 4, we describe the on-site meteorological characteristics during the one-year study period as well as how wind and turbulence characteristics varied as a function of height within and above the forest canopy throughout the year. We then use the meteorological and micrometeorological measurements to evaluate the applicability of the HOST hypothesis and examine its appropriateness as a function of ABL regime (i.e., the daytime convective boundary layer (CBL) versus the NBL), season (i.e., summer versus winter), different wind directions, and atmospheric stability regimes (i.e., very unstable regimes and very stable regimes that we define using SL stability parameters).

2. Site description and datasets

2.1. Site description

We used observations obtained from a 60-m flux tower located near Oak Ridge, Tennessee, U.S. to evaluate the applicability of HOST within and above the forest canopy (Fig. 1a). This region of the Tennessee Valley is characterized by mountain ridges oriented southwest to northeast with a relief of a couple of hundred meters above the valley

Table 1
Percent data completion of horizontal wind speed ($\overline{U}$), friction velocity (u_*), and turbulent kinetic energy (*TKE*) at each sampling height (in m AGL and as a function of canopy height, i.e. z/h_c, where h_c is the average canopy height of 25 m AGL) at the Chestnut Ridge tower in 2016, following the removal of time periods containing missing or physically-unrealistic values, as well as instances when $90° \leq WD \leq 135°$ when the tower impacted the measurements.

Sampling Height (m AGL)	z/h_c	% Complete $\overline{U}$	% Complete u_*	% Complete *TKE*
5	0.2	75.3	61.0	69.2
10	0.4	75.8	65.0	69.7
15	0.6	74.5	68.3	69.4
25	1.0	76.7	75.3	75.8
30	1.2	76.7	75.5	76.0
35	1.4	64.2	57.9	60.3
40	1.6	76.0	74.0	74.7
45	2.0	70.2	68.3	68.8

floor (Fig. 1b). The Cumberland Plateau, with ridgetops up to around 1000 m MSL, is about 20 km to the west and north of Chestnut Ridge. The taller Smoky Mountains are located to the south and east of the Chestnut Ridge, and the tallest peaks of the Smoky Mountains, which are over 2000 m MSL, are about 80 km southeast of Chestnut Ridge .

The tower (35.9311°N, 84.3323°W, 371 m above mean sea level (MSL); Fig. 1c) at Chestnut Ridge was installed in 2005 and is part of the NOAA Air Resources Laboratory Atmospheric Turbulence and Diffusion Division's Surface Energy Budget Network (SEBN) and is also included in the AmeriFlux network (site identification: US-ChR; e.g., Meyers, 2016). The tower is on the reservation of the Department of Energy's Oak Ridge National Laboratory, and the tower is located within a mixed hardwood deciduous forest, consisting of oak, hickory, tulip poplar, and maple trees. The mean height of the canopy, h_c, in the immediate vicinity of the tower is 25 ± 3 m (Wilson et al., 2012). We refer the reader to Hanson and Wullschleger (2003); Wilson and Meyers (2007) and Wilson et al. (2012) for more details about the site.

2.2. Turbulent flux profiles

Turbulence quantities were sampled at Chestnut Ridge using RM Young sonic anemometers (model number 81000VRE). These anemometers were installed on a 2 m boom extending outward from the northwest corner of the tower at eight different sampling heights. Measurements were made both within (i.e., 5 m, 10 m, and 15 m above ground level (AGL)) and above (i.e., 25 m, 30 m, 35 m, 40 m, and 45 m AGL) the forest canopy at a frequency of 10 Hz. To better place our results into the context of previous studies, we normalized each of these heights by h_c to obtain z/h_c. Prior to computing the turbulence statistics at 15 min intervals at each of the sampling heights, we applied standard coordinate rotations and corrections to the datasets. These corrections have been previously documented in, for example Meyers (2001); Meyers and Baldocchi (2005); Lee et al. (2019).

We used the turbulence measurements from Chestnut Ridge to compute u_* and V_{TKE}. The friction velocity was calculated as

$$u_* = \sqrt[4]{(\overline{u'w'})^2 + (\overline{v'w'})^2} \quad (1)$$

where $\overline{u'w'}$ and $\overline{v'w'}$ are the covariances between the vertical wind (w) and the horizontal (u) and meridional (v) wind, respectively.

Furthermore, we computed the turbulence velocity scale, V_{TKE}, as

$$V_{TKE} = \sqrt{TKE} = \sqrt{0.5(\overline{u'^2} + \overline{v'^2} + \overline{w'^2})} \quad (2)$$

In Eq. (2), $\overline{u'^2}$, $\overline{v'^2}$, and $\overline{w'^2}$ are the variances of the u, v, and w wind components, respectively.

After computing the turbulence parameters and, using the same criteria as was used by, for example Lee et al. (2023b), we removed physically-unrealistic values, which we defined as $\overline{U} > 30\ m\ s^{-1}$, $u_* > 2\ m\ s^{-1}$, and $TKE > 10\ m^2\ s^{-2}$. Because previous studies have well documented the impact of tower-induced impacts on in situ turbulence

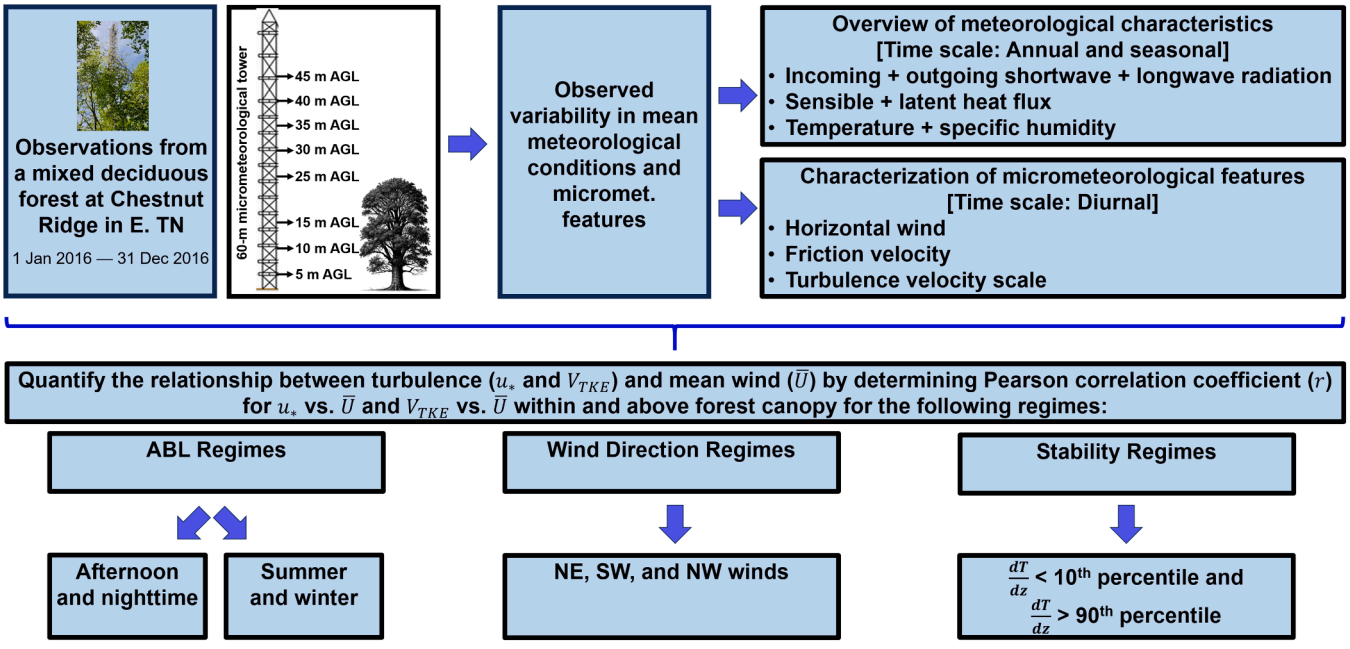

Fig. 2. Flowchart summarizing the observations, meteorological, and micrometeorological features explored, approach, and conceptual framework employed in this study to evaluate HOST for different ABL, *WD*, and atmospheric stability regimes.

measurements, (e.g., McCaffrey et al., 2017), we also removed periods when the wind direction (*WD*) was between 90° and 135° because, as noted earlier in this section, the sonic anemometers used to measure the turbulence quantities were installed on the northwest corner of the tower. On average, 73.7 %, 68.1 %, and 70.5 % of the $\overline{U}$, u_*, and *TKE* data, respectively, were available at the different sampling heights following the removal of physically-unrealistic values and times when *WD* was between 90° and 135° Measurements from 35 m AGL had the least complete data record due to data gaps in the measurement record; 64.2 %, 57.9 %, and 60.3 % of the data 35 m AGL were available for $\overline{U}$, u_*, and *TKE*, respectively (Table 1). To compute the means across select time periods, we only considered the data for a given time period and sampling height if at least 75 % of the data were available for that given variable and time period following previous work (e.g., Lee et al., 2023a, 2024).

2.3. Ancillary measurements

Along with the vertical profile of turbulence measurements at Chestnut Ridge in 2016, three collocated platinum resistance thermometers (PRTs) were used to measure temperature at each of the sampling heights referenced in Section 2.2. The PRTs were enclosed within the same fan-aspirated shield at each sampling height, and 15-min means of these values were calculated at each sampling height for consistency with the averaging timescale for the wind and turbulence measurements introduced in Section 2.2.

Other measurements at the tower included radiation and flux measurements that are part of the SEBN and that were used to characterize the near-surface atmospheric conditions during the study period. These measurements included air temperature and relative humidity measured at 43 m AGL using a Thermometrics Corp PRT and Vaisala 50Y, respectively, and incoming and outgoing shortwave and longwave radiation measured at 36 m AGL using a Kipp&Zonen CNR1. The eddy covariance system, which includes an RM Young 81000 V sonic anemometer and a LI-COR 7500 infrared gas analyzer for measuring CO_2 and H_2O mixing ratios, was installed at 43 m AGL and sampled at 10 Hz to compute 30-min sensible heat flux (*H*) and latent heat flux (*LE*).

3. Methods

3.1. Approach to evaluate the HOST hypothesis

After implementing the data quality assurance and data quality control procedures for each of the datasets discussed in Section 2, we used the suite of turbulence and meteorological measurements to evaluate the applicability of HOST at the site under varying near-surface atmospheric conditions. To this end, we determined the relationship between u_* and $\overline{U}$, as well as between V_{TKE} and $\overline{U}$, and quantified this relationship by computing the Pearson correlation coefficient (*r*). As summarized in Fig. 2, we performed this evaluation for three different classifications: ABL regimes, *WD* regimes, and atmospheric stability regimes.

3.2. Evaluation of HOST for different ABL regimes and seasons

To distinguish among different ABL regimes, we contrasted daytime ABLs with nighttime ABLs by differentiating two regimes:

1. Daytime ABLs, whereby we used observations obtained during the afternoon when the ABL is typically quasi-stationary, i.e. between 1200 and 1600 LST (LST = UTC – 5)
2. Nighttime ABL (i.e., NBL), during which the ABL is typically stable, whereby we used observations between 0000 and 0400 LST.

We performed these analyses using observations obtained from two contrasting seasons and thus used observations obtained from January and July 2016 (i.e., representative winter and summer months for the northern hemisphere). Sensitivity tests (not shown) with other months in the winter and summer indicated that our results were not sensitive to our choice of month in these respective seasons. At the site in January, the leaf area index (LAI) is around 1 $m^2\ m^{-2}$, following the approach discussed in Wilson and Meyers (2007). In July, the LAI is typically around 5 $m^2\ m^{-2}$, but can be as large as 6 $m^2\ m^{-2}$ during other years. Normalized Difference Vegetation Index (NDVI), derived from the Moderate Resolution Imaging Spectroradiometer (MODIS), ranged from ~ 0.45 in January 2016 to ~ 0.9 in July 2016.

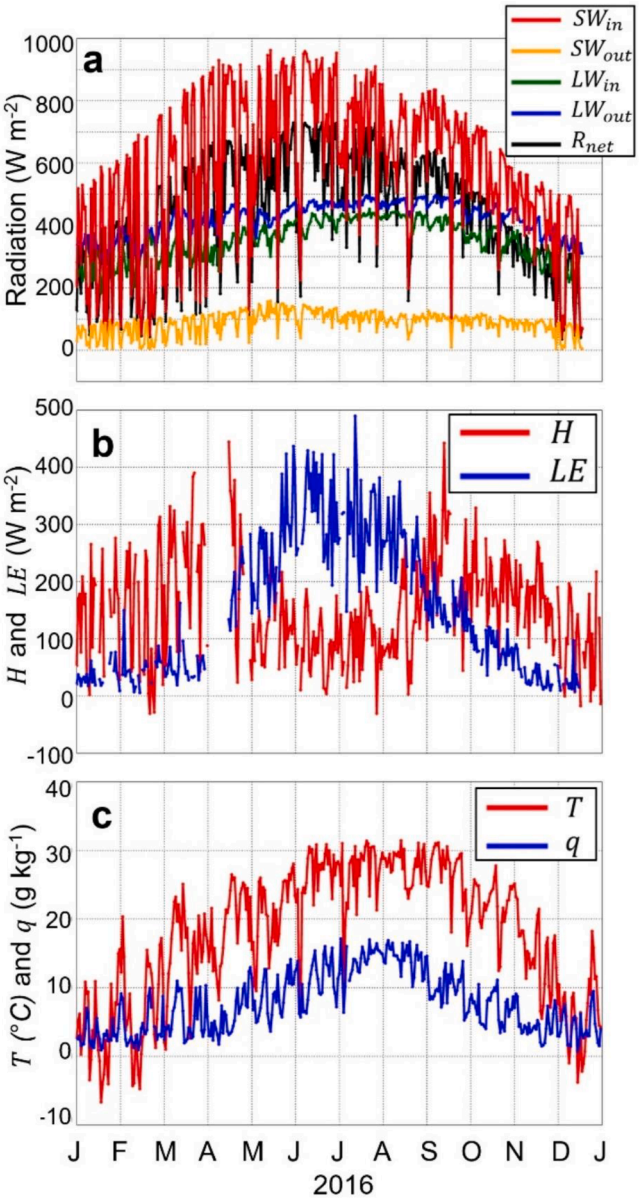

Fig. 3. (a) Annual cycle of the mean afternoon (1200–1600 LST) incoming shortwave radiation (SW_{in}; red line), outgoing shortwave radiation (SW_{out}; orange line), incoming longwave radiation (LW_{in}; green line), outgoing longwave radiation (LW_{out}; blue line), and net radiation (R_{net}; black line) at Chestnut Ridge in 2016. Same for panel (b), but for *H* (red line) and *LE* (blue line), and for panel (c), but for air temperature (*T*; red line) and specific humidity (*q*; blue line). Note that the radiation and flux measurements are missing during the latter half of December and during the first half of April, respectively.

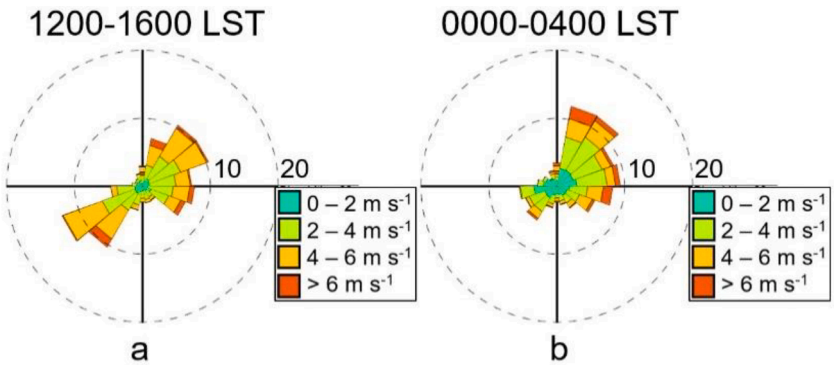

Fig. 4. Wind rose for (a) 1200–1600 LST and (b) 0000–0400 LST for 1 January through 31 December 2016, using observations from 45 m AGL (i.e., $1.8h_c$). Turquoise, light green, orange, and red correspond with $\overline{U} < 2\ m\ s^{-1}$, $2 - 4\ m\ s^{-1}$, $4 - 6\ m\ s^{-1}$, and $> 6\ m\ s^{-1}$, respectively. A *WD* bin size of 20° is used in each of the plots.

3.3. Evaluation of HOST under different wind directions

Because different wind directions over both valleys and ridges have been found to be critical for ABL and turbulence regimes and tracer mixing over complex terrain (e.g., Pal et al., 2014; Pal et al., 2017) and adjacent plains (e.g., Pal and Lee, 2019; Anand and Pal, 2023), we evaluated HOST under the following subsets of prevailing wind regimes:

1. Northeast (NE) winds (i.e., $0° \leq WD < 90°$)
2. Southwest (SW) winds (i.e., $180° \leq WD < 270°$)
3. Northwest (NW) winds (i.e., $270° \leq WD < 360$)

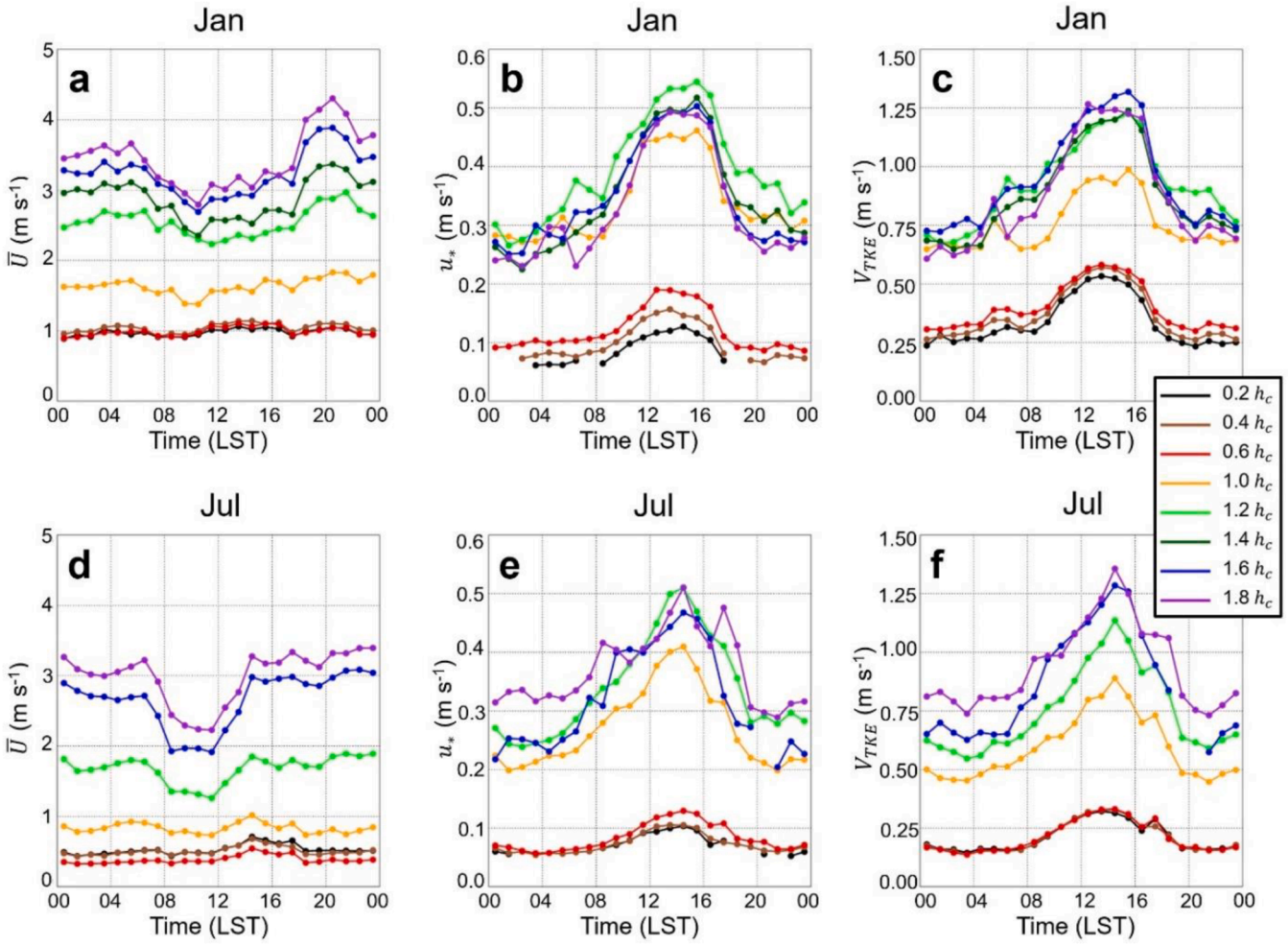

Fig. 5. Mean diurnal cycle of (a) $\overline{U}$, (b) u_*, (c) and V_{TKE} as a function of local time of day for January 2016. Same for panels (d) – (f), but for July 2016. The colors of the different lines represent the different heights (see figure legend). Not all data are shown because of < 75 % data completion at certain times of day in the mean diurnal u_* cycles.

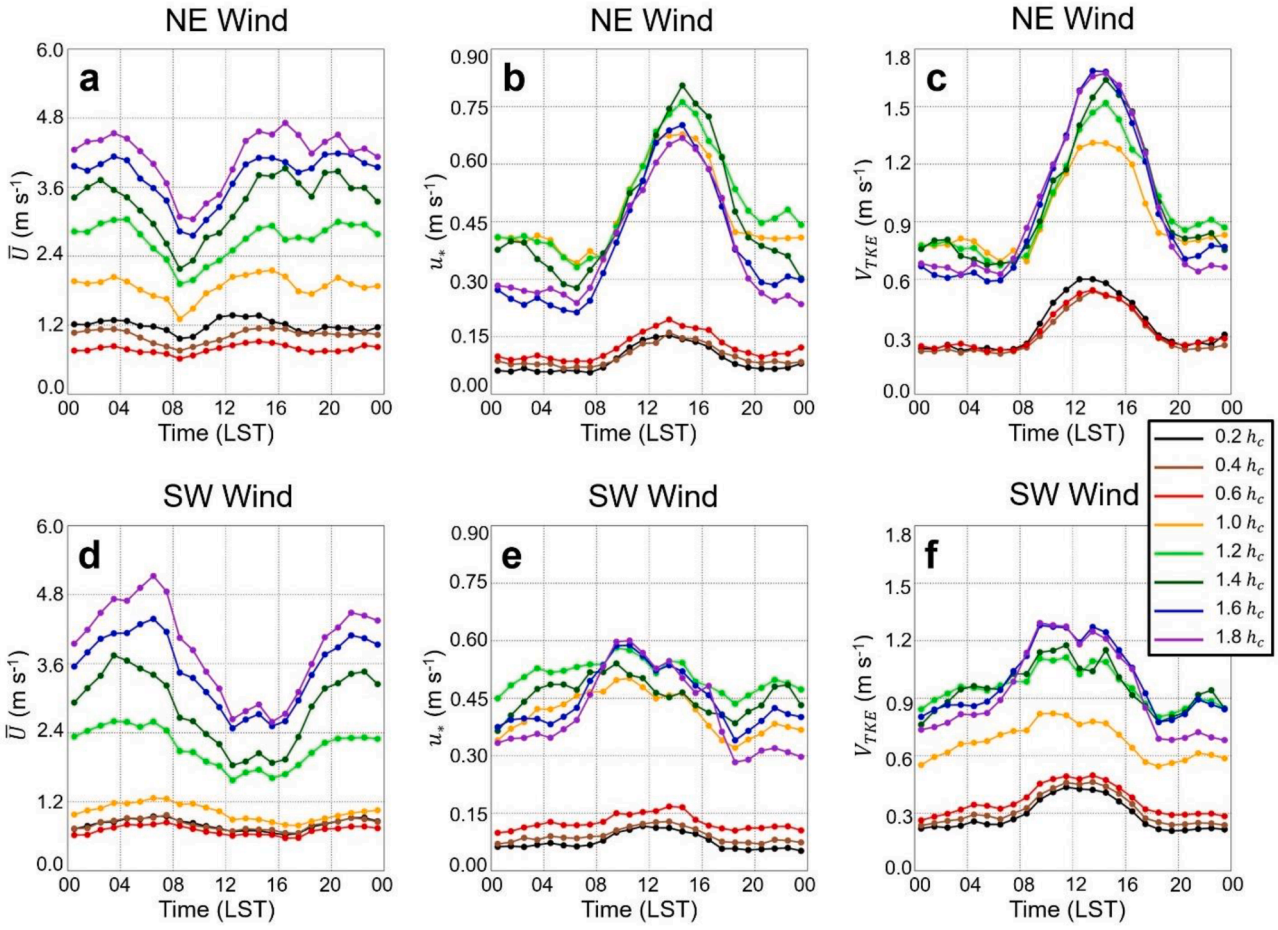

Fig. 6. Mean diurnal cycle of (a) $\overline{U}$, (b) u_*, and (c) V_{TKE} as a function of local time of day on days with NE winds (i.e., $0° \leq WD < 90°$). Same for panels (d) – (f), but on days with SW winds (i.e., $180° \leq WD < 270°$). The colors of the different lines represent the different heights (see figure legend).

Note that we excluded southeast (SE) winds, defined as wind directions between 90° and 180°, to remove any impacts of the tower, and we conducted these analyses irrespective of time of day or season.

3.4. Evaluation of HOST for different atmospheric stability regimes

We distinguished among different near-surface atmospheric stability regimes by computing temperature gradients (e.g., Sedefian and Bennet, 1980; Mohan and Siddiqui, 1998). Different stability regimes were determined by calculating the temperature gradient, $\frac{dT}{dz}$ (e.g., Stull, 1988), which we did by determining the slope of the best-fit line between all temperature measurements available at a given timestep and height. Sensitivity tests (not shown) for computing $\frac{dT}{dz}$ as a function of different heights within and above the forest canopy indicated that our results were independent to the metric used to compute $\frac{dT}{dz}$. Over the entire year, $\frac{dT}{dz}$ ranged from $-0.100\ K\ m^{-1}$ to $0.086\ K\ m^{-1}$; in January (July) $\frac{dT}{dz}$ ranged from $-0.047\ K\ m^{-1}$ ($-0.059\ K\ m^{-1}$) to $0.080\ K\ m^{-1}$ ($0.070\ K\ m^{-1}$). To evaluate HOST under different stability conditions, we contrasted two stability extremes:

1. Highly-unstable regimes, in which $\frac{dT}{dz}$ was below the 10th percentile of all values of $\frac{dT}{dz}$ (i.e., $\frac{dT}{dz} < -0.038\ K\ m^{-1}$)
2. Highly-stable regimes, in which $\frac{dT}{dz}$ exceeded the 90th percentile of all values of $\frac{dT}{dz}$ (i.e., $\frac{dT}{dz} > 0.019\ K\ m^{-1}$).

4. Results and discussion

4.1. Meteorological characteristics at Chestnut Ridge in 2016

During the study period, mean afternoon (i.e., 1200–1600 LST) incoming shortwave radiation ranged from ~ 500 $W\ m^{-2}$ in January to ~ 950 $W\ m^{-2}$ in June, and net radiation, which is defined as the sum of the difference between incoming and outgoing shortwave radiation and longwave radiation, peaked near 700 $W\ m^{-2}$ in June (Fig. 3a). Mean afternoon H exceeded LE during the cool season, but from about late April through early September, LE was a larger component of the surface energy balance than H (Fig. 3b). Larger LE than H during the summer is a pattern that is consistent with previously-reported findings from within the immediate study region (e.g., Wilson and Baldocchi, 2000; Wilson

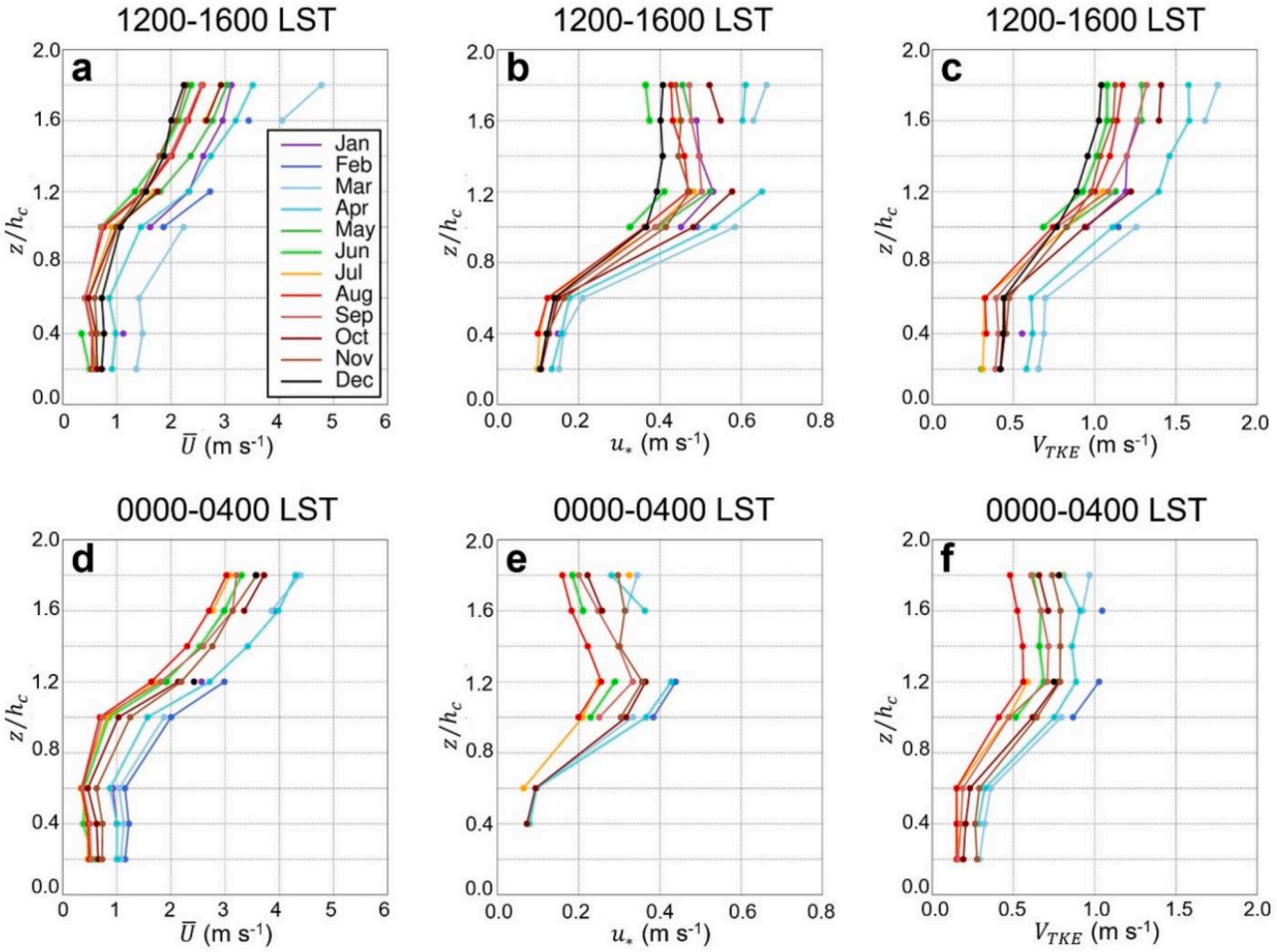

Fig. 7. Mean vertical profiles (a) $\overline{U}$, (b) u_*, and (c) V_{TKE} as a function of month and averaged between 1200 and 1600 LST. Same for panels (d) – (f) but for 0000–0400 LST. Note that not all data are shown for all sampling heights for all variables because of <75 % data completion within several of these time periods (cf. Section 2) including, for example afternoon $\overline{U}$, u_*, and V_{TKE} at $1.4h_c$.

et al., 2000), as well as with findings from other forested monitoring sites located in the Southeast U.S. (e.g., Lee et al., 2012; Lee et al., 2015) and elsewhere in the continental U.S. (e.g., Greco and Baldocchi, 1996; Yi et al., 2001; Wilson et al., 2002). Due to the comparatively large on-site *LE* during the summer, mean daily specific humidity reached a maximum of about 15 $g\,kg^{-1}$ during this time (Fig. 3c). During the study period, mean daily temperatures ranged from around 2 °C in January to 30 °C during the summer (Fig. 3c).

We used long-term climatological observations from the city of Oak Ridge, Tennessee, located about 12 km northeast of the site, to provide climatological context for the meteorological observations obtained from 2016 at Chestnut Ridge. Based on 20-year means obtained between 2000 and 2019, the mean annual temperature was 15.5 °C, and the mean annual precipitation was 143 cm. 2016 was slightly warmer and drier than the 20-year mean, as the mean annual temperature and total precipitation was 16.6 °C and 122 cm, respectively.

4.2. *Wind and turbulence characteristics at Chestnut Ridge in 2016*

4.2.1. *Diurnal variability in wind direction*

Throughout 2016, the wind direction measured at the uppermost sampling height (i.e., $1.8h_c$, or 45 m AGL) during the afternoon showed a bimodal distribution, with NE and SW winds being the most prevalent directions. During the nighttime, however, NE winds were most dominant (Fig. 4b). To investigate whether this diurnal wind shift has seasonal dependence, we performed the same analyses separately for January and July but found no clear evidence of seasonal variations in wind direction during these periods (results not shown). The absence of a diurnal wind shift is perhaps not surprising and suggests that any locally-generated slope flows are typically overwhelmed by larger-scale (i.e., mesoscale- to synoptic-scale) flows within the region. In other words, the synoptic forcing here often outweighs localized thermally-driven or local, terrain-induced flows.

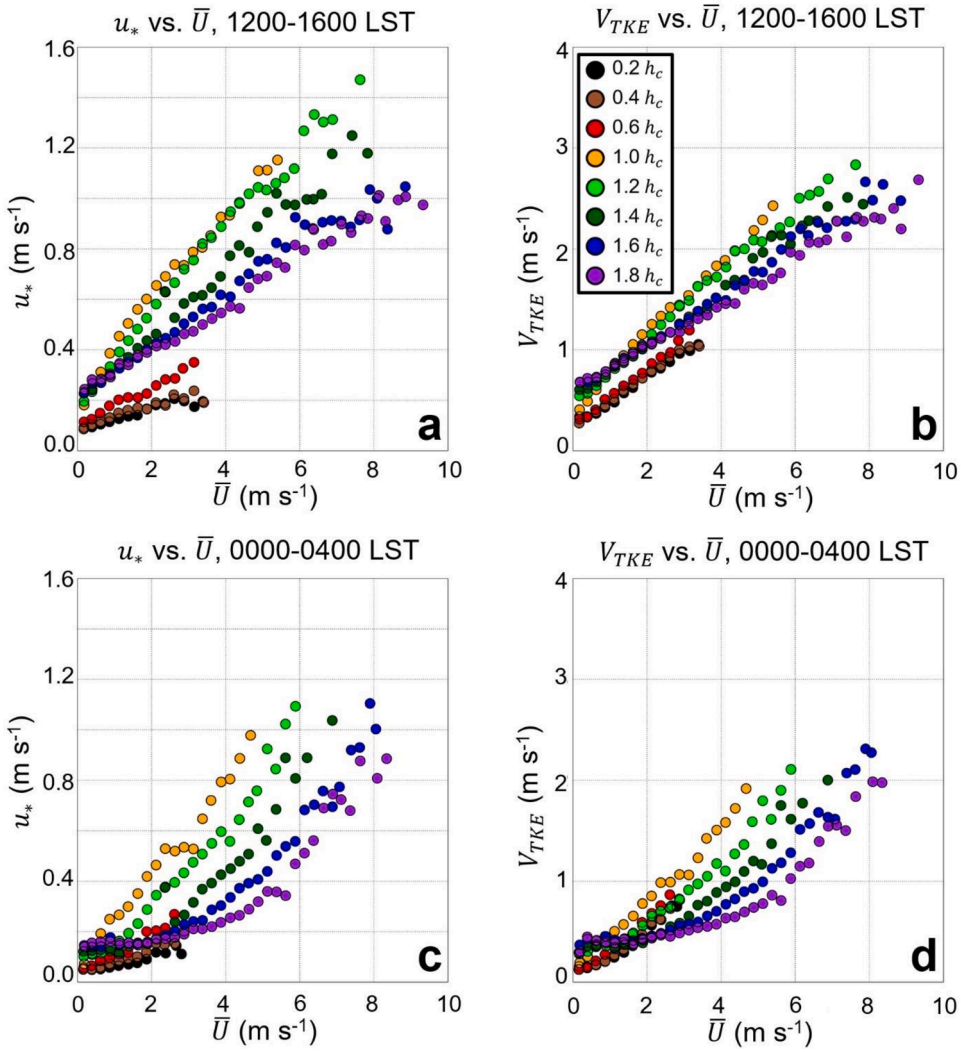

Fig. 8. (a) Mean u_* as a function of $\overline{U}$ for 1200–1600 LST between 1 January 2016 and 31 December 2016. Same for (b) but for V_{TKE}. Panels (c) and (d) show the relationship between u_* and $\overline{U}$ and between V_{TKE} and $\overline{U}$, respectively, but for 0000–0400 LST. The colors of the different symbols represent the different heights (see figure legend). A bin size of 0.25 $m\ s^{-1}$ is used in all panels.

4.2.2. Mean diurnal cycles of wind speed and turbulence

When we considered the seasonal mean diurnal cycles of $\overline{U}$, u_*, and V_{TKE} as a function of different seasons, we found that the mean wind speeds were about 0.5 $m\ s^{-1}$ larger in winter (January in this example, Fig. 5a) and roughly 0.5 $m\ s^{-1}$ smaller in summer (July in this example, Fig. 5d) than the mean diurnal cycle averaged across the entire year. Furthermore, the diurnal $\overline{U}$ minimum occurred a couple of hours later in January than the mean diurnal cycle over the entire year. Similarly, January values for u_* and V_{TKE} were larger during the winter (Fig. 5b and c, respectively) than during the summer (Fig. 5e and 5f, respectively). There were also large differences in $\overline{U}$, u_*, and V_{TKE} at the different sampling heights in January and July, with three distinctive regimes present in both of these months:

1. $0.0h_c$ – ~ $0.6h_c$
2. ~ $1.0h_c$
3. ~ $1.2h_c$ – $1.8h_c$

These three regimes confirm the large impacts of the canopy on the kinematic and turbulence measurements at the site.

We further analyzed the mean diurnal cycles of $\overline{U}$, u_*, and V_{TKE} as a function of time of day when the wind direction was from a given sector, which we defined as NE winds (i.e., $0° \leq WD < 90°$), SW winds (i.e., $180° \leq WD < 270°$), and NW winds (i.e., $270° \leq WD < 360$). Note that we did not investigate the role of SE winds because of the tower's influence on the turbulence characteristics when the winds were from this particular wind direction (cf. Section 2.2). In order for a day to be

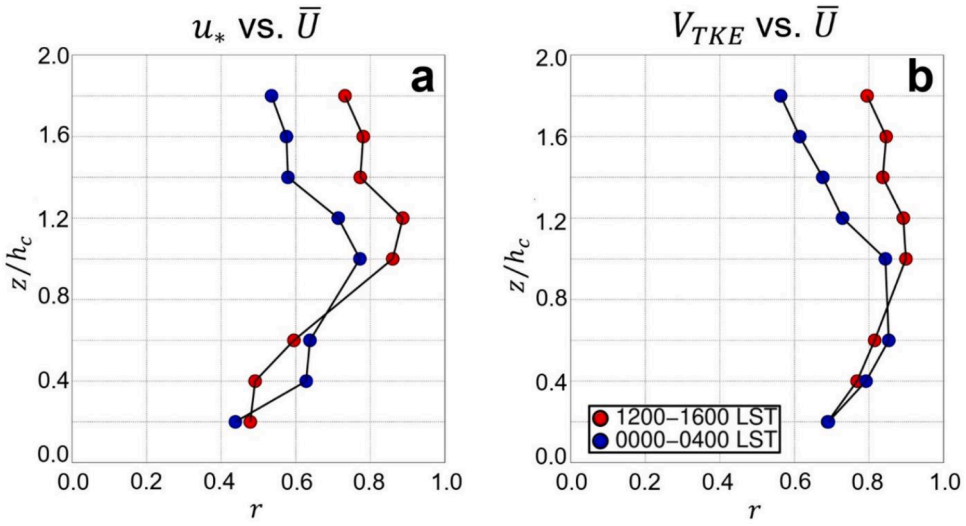

Fig. 9. Pearson correlation coefficient (r) as a function of z/h_c between (a) u_* and $\overline{U}$ and between (b) V_{TKE} and $\overline{U}$ for 1200–1600 LST (red circles) and 0000–0400 LST (blue circles). All values shown are statistically significant at the 0.01 confidence level (i.e., $p < 0.01$).

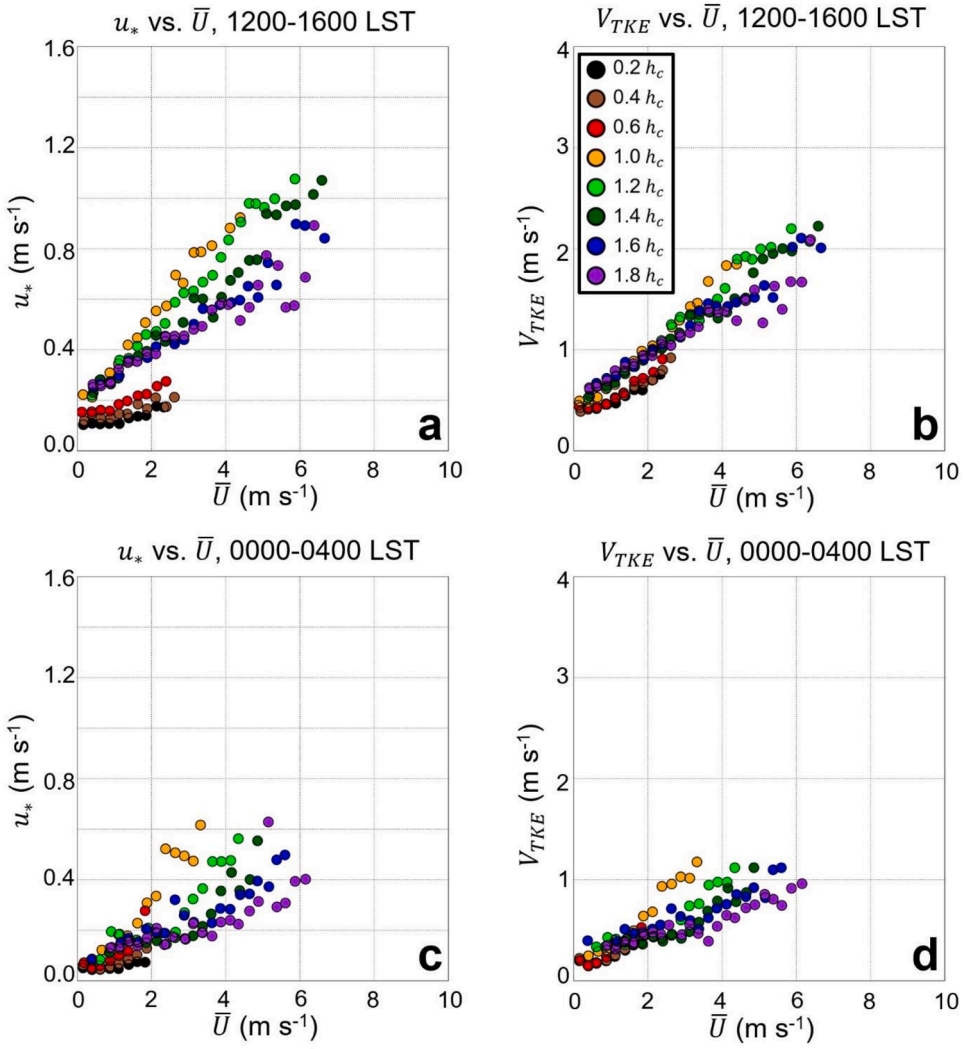

Fig. 10. (a) Mean u_* as a function of $\overline{U}$ for 1200–1600 LST in January 2016. Same for (b) but for V_{TKE}. Panels (c) and (d) show the relationship between u_* and $\overline{U}$ and between V_{TKE} and $\overline{U}$, respectively, but for 0000–0400 LST. The colors of the different symbols represent the different heights (see figure legend). A bin size of 0.25 $m\ s^{-1}$ is used in all panels.

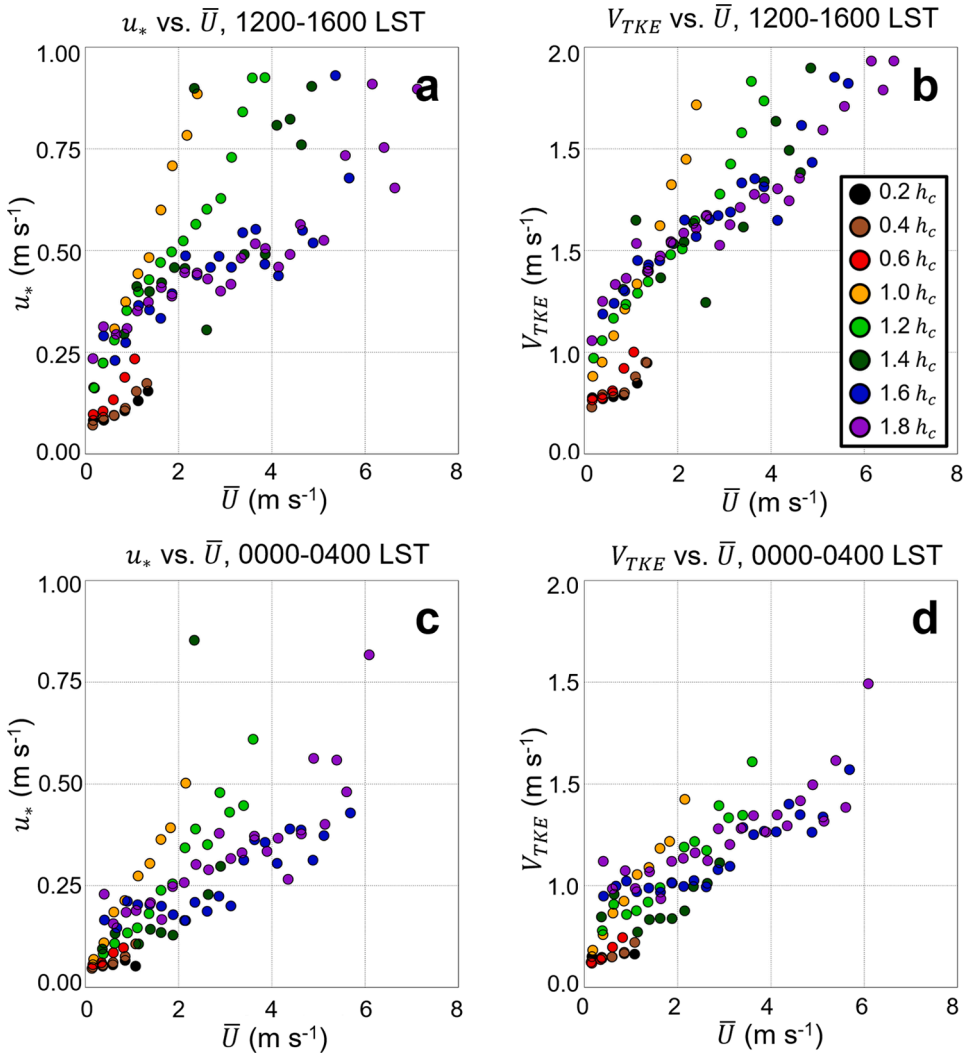

Fig. 11. (a) Mean u_* as a function of $\overline{U}$ for 1200–1600 LST in July 2016. Same for (b) but for V_{TKE}. Panels (c) and (d) show the relationship between u_* and $\overline{U}$ and between V_{TKE} and $\overline{U}$, respectively, but for 0000–0400 LST. The colors of the different symbols represent the different heights (see figure legend). A bin size of 0.25 $m\ s^{-1}$ is used in all panels.

considered as having winds from these respective directions, at least 90 % of the observations had to align with the given direction, although our results were not strongly sensitive to our choice of these thresholds. Over the one-year study period, there were 17 (20) days with constant NW (SW) winds throughout the day. Only one day had constant NW winds and, due to the small sample size, this day was not shown in the composite mean diurnal cycles of $\overline{U}$, u_*, and V_{TKE} shown in Fig. 6. We found that $\overline{U}$ was generally larger on days with NE winds than on days with SW winds. Consequently, u_* and V_{TKE} were larger, and these quantities showed a sharper daytime maximum on the subset of days with NE winds than the composites of days with SW winds.

When placing the results presented here into the context of findings from previous studies, we found that the magnitude of the wind speeds and turbulence quantities (i.e., u_* and V_{TKE}) were generally smaller than those reported at other study locations, although we caution here that other physical factors, for example land-surface heterogeneities and seasonality, can affect how our observations compare with findings presented in other studies. Rigden et al. (2018) used observations from different land cover types within the AmeriFlux network and found that, when averaged over 11 deciduous forests sites, u_* varied from about 0.3 $m\ s^{-1}$ in the morning to about 0.5 $m\ s^{-1}$ during the afternoon. Lee et al. (2015), using four years of observations obtained from a mixed deciduous ridgetop in central Virginia located about 600 km northeast of Chestnut Ridge, found that $\overline{U}$ sampled approximately 3 m above the canopy top was lower in the summer than in the winter which is consistent with findings from Chestnut Ridge. In contrast, though, Lee et al. (2015) found that $\overline{U}$ was typically around 5 $m\ s^{-1}$ and 2.5 $m\ s^{-1}$ in the winter and summer, respectively, and $\overline{U}$ was oftentimes lower during the daytime than during the nighttime.

4.2.3. Variability in wind and turbulence profiles as a function of time of year

The typical observed vertical variability in the turbulence parameters and mean wind exhibited similar features during daytime and

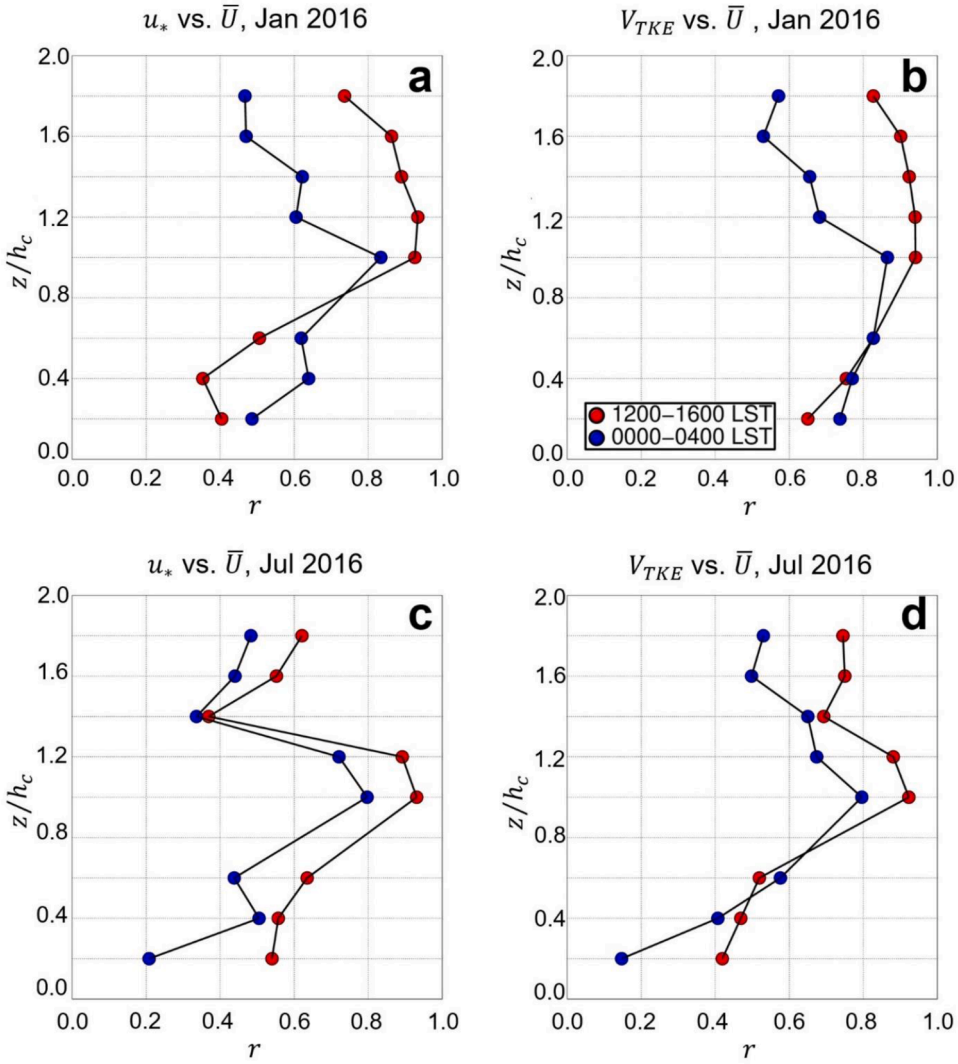

Fig. 12. Pearson correlation coefficient (r) as a function of z/h_c between (a) u_* and $\overline{U}$ and between (b) V_{TKE} and $\overline{U}$ for 1200–1600 LST (red circles) and 0000–0400 LST (blue circles) in January 2016. Same for panels (c) and (d), respectively, but for July 2016. All values shown are statistically significant at the 0.01 confidence level (i.e., $p < 0.01$).

nighttime (i.e., lower (higher) values within (above) the canopy, and an inflection point near h_c). Additionally, when considering the evolution of the vertical profiles of $\overline{U}$, u_*, and V_{TKE} as a function of time of day and time of year, we found negligible differences between in-canopy afternoon values (i.e., between 1200 and 1600 LST) of $\overline{U}$, when the ABL is typically quasi-stationary (Fig. 7a), and in-canopy nighttime values (i.e., between 0000 and 0400 LST), when the ABL is typically stable (Fig. 7d). These findings were consistent with the mean diurnal cycle shown in Fig. 4. Above-canopy values of $\overline{U}$ were about 0.5 $m\,s^{-1}$ larger during the nighttime hours than afternoon hours, and the largest differences between nighttime and afternoon occurred during the late fall and early winter at the site. Afternoon values of u_* were considerably larger than nighttime u_* (Fig. 7b, 7e); in-canopy differences varied little as a function of time of year and were generally 0.05–0.10 $m\,s^{-1}$ lower during the nighttime than afternoon. Above the canopy, the mean differences were as large as 0.3 $m\,s^{-1}$ which typically occurred during the spring and fall. The profiles of V_{TKE} showed similar characteristics to u_*; the largest in-canopy differences between the afternoon and nighttime generally happened in the spring when V_{TKE} was on average 0.3 $m\,s^{-1}$ larger than the nighttime values. In the summer, mean differences were about half this value (Fig. 7c, 7f).

4.3. *Relationship between turbulence and wind speed as a function of time of day*

When examining the dependence of u_* and V_{TKE} on $\overline{U}$ at different heights during different times of the day, we found a strong linear relationship between u_* and $\overline{U}$ (Fig. 8a) and between V_{TKE} and $\overline{U}$ during the afternoon (Fig. 8b). When considering only nighttime values, we found a linear relationship between u_* and $\overline{U}$ (Fig. 8c) and V_{TKE} and $\overline{U}$

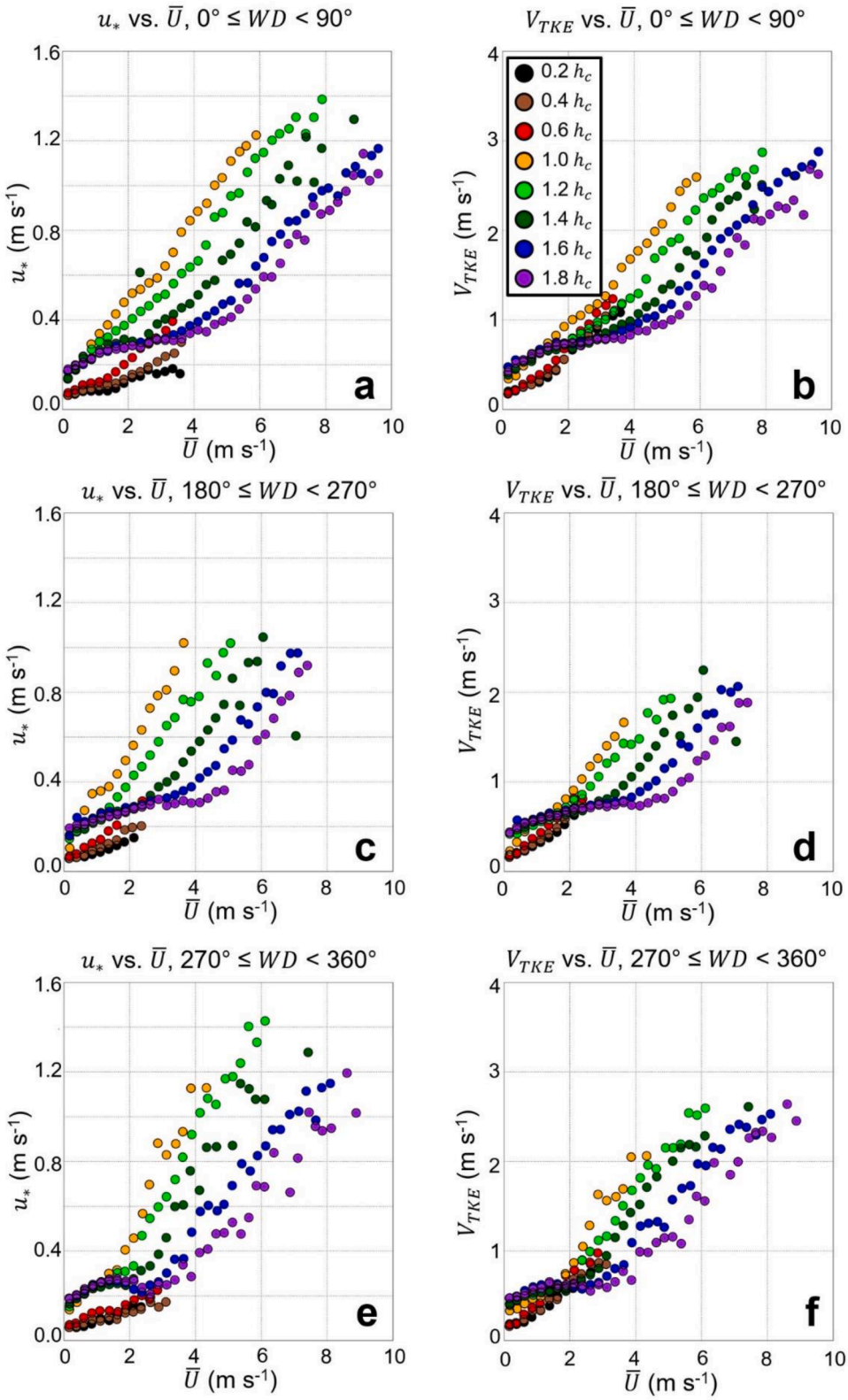

Fig. 13. (a) Mean u_* as a function of $\overline{U}$ for cases when $0^\circ \leq WD < 90^\circ$ Same for (b) but for V_{TKE}. Same for (c) and (d) and for (e) and (f), but for instances in which $180^\circ \leq WD < 270^\circ$ and $270^\circ \leq WD < 360^\circ$, respectively. The colors of the different symbols represent the different heights (see figure legend). A bin size of 0.25 $m\ s^{-1}$ is used in all panels.

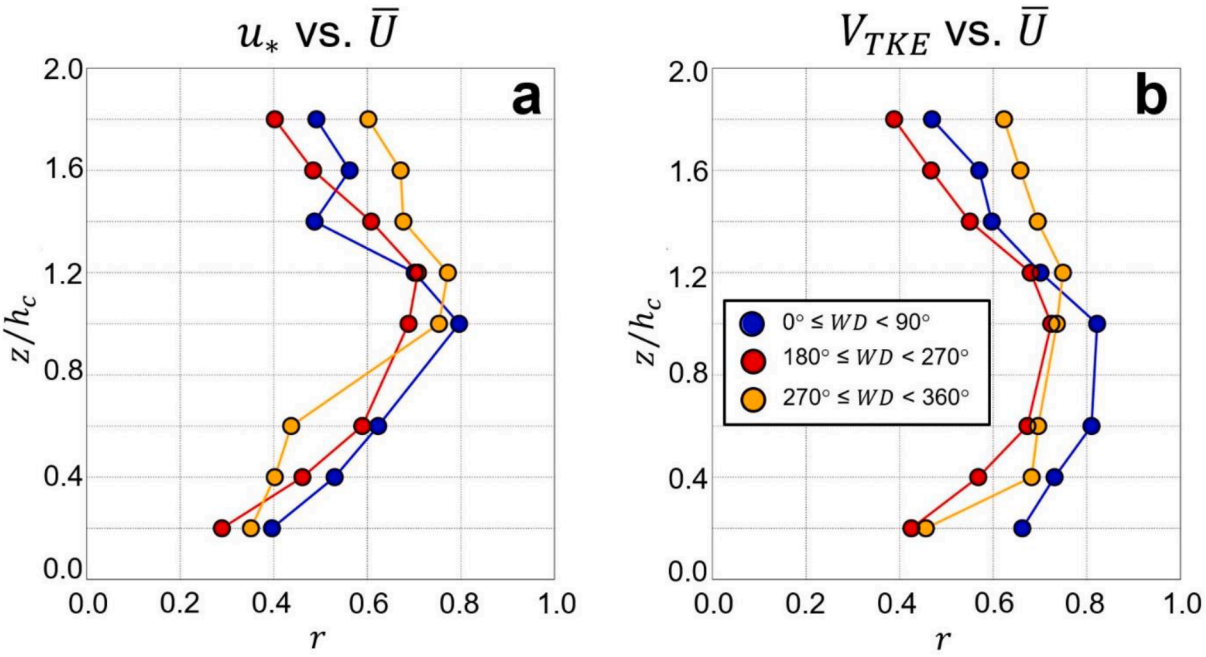

Fig. 14. Pearson correlation coefficient (r) as a function of z/h_c between (a) u_* and $\overline{U}$ and between (b) V_{TKE} and $\overline{U}$ for cases when $0° \leq WD < 90°$ (green circles), $90° \leq WD < 180°$ (blue circles), $180° \leq WD < 270°$ (red circles) and $270° \leq WD < 360°$ (orange circles). All values shown are statistically significant at the 0.01 confidence level (i.e., $p < 0.01$).

Table 2
Slope between u_* vs. $\overline{U}$ for stable regimes, u_* vs. $\overline{U}$ for unstable regimes, V_{TKE} vs. $\overline{U}$ for stable regimes, and V_{TKE} vs. $\overline{U}$ for unstable regimes for different z/h_c.

z/h_c	u_* vs. $\overline{U}$, Stable Regimes	u_* vs. $\overline{U}$, Unstable Regimes	V_{TKE} vs. $\overline{U}$, Stable Regimes	V_{TKE} vs. $\overline{U}$, Unstable Regimes
0.2	0.02	0.05	0.10	0.26
0.4	0.02	0.05	0.13	0.27
0.6	0.05	0.08	0.18	0.31
1.0	0.13	0.21	0.24	0.40
1.2	0.10	0.20	0.15	0.37
1.4	0.06	0.16	0.11	0.30
1.6	0.03	0.12	0.06	0.27
2.0	0.02	0.10	0.05	0.23

(Fig. 8d) up to about $1.2h_c$. Above this height, these relationships were non-linear. For example, at $1.8h_c$ there was only a small increase in V_{TKE} with increasing wind speeds up to about 4 $m\,s^{-1}$. Above the $\sim 4\ m\,s^{-1}$ $\overline{U}$ threshold, the relationship between V_{TKE} and $\overline{U}$ became approximately linear, and larger V_{TKE} corresponded with larger $\overline{U}$.

Another important feature that was revealed by the analyses (Fig. 9) includes larger u_* for the same $\overline{U}$ at h_c compared to any other tower levels (i.e., the orange circles in Fig. 9) across all wind speeds. These results suggest the presence of maximum turbulence exchanges at h_c, which is the interface between the within-canopy and above-canopy layers, and is analogous to turbulence exchanges occurring at the entrainment zone located at the interface between the turbulent ABL and overlying laminar free atmosphere.

To better elucidate the linear relationship that exists between the different turbulence quantities and wind speed, we computed r for the afternoon and nighttime. We found that in-canopy nighttime values of r were consistently larger than afternoon r values, both for the relationship between u_* and $\overline{U}$ (Fig. 9a) and the relationship between V_{TKE} and $\overline{U}$ (Fig. 9b). Above the canopy, the opposite pattern was present, as the relationship between afternoon u_* and $\overline{U}$, as well as between afternoon V_{TKE} and $\overline{U}$, was more linear than within the canopy, with $r > 0.7$ ($p < 0.01$) and $r > 0.8$ ($p < 0.01$), respectively. In contrast, r values during the nighttime hours were much lower at all above-canopy sampling heights, indicative of a less-linear relationship, both for u_* versus $\overline{U}$ and for V_{TKE} versus $\overline{U}$. Also apparent from these analyses is that the strongest linear relationships between u_* and $\overline{U}$, and between V_{TKE} and $\overline{U}$, occur at the top of the canopy during both the afternoon and the nighttime where turbulence changes appear maximized (cf. Fig. 8).

4.4. Relationship between turbulence and wind speed as a function of season

As discussed in the previous sections, we found there were considerable differences in how $\overline{U}$, u_*, and V_{TKE} varied as a function of height within the different months during the study period. Therefore, in this section, we evaluate how the relationships between u_* and $\overline{U}$, and between V_{TKE} and $\overline{U}$, varied between two contrasting seasons. As we noted in Section 3, we contrast these relationships between when the canopy is not foliated versus when the canopy is fully foliated (based on LAI and NDVI estimates and phenological observations from the site) using observations obtained from Chestnut Ridge in January and July, respectively.

When we compared the relationships between u_* and $\overline{U}$ and between V_{TKE} and $\overline{U}$ in January versus July, we found that the relationship was linear during the afternoon, and there was less scatter present in this relationship in January (Figs. 10a, and b) than was present in July

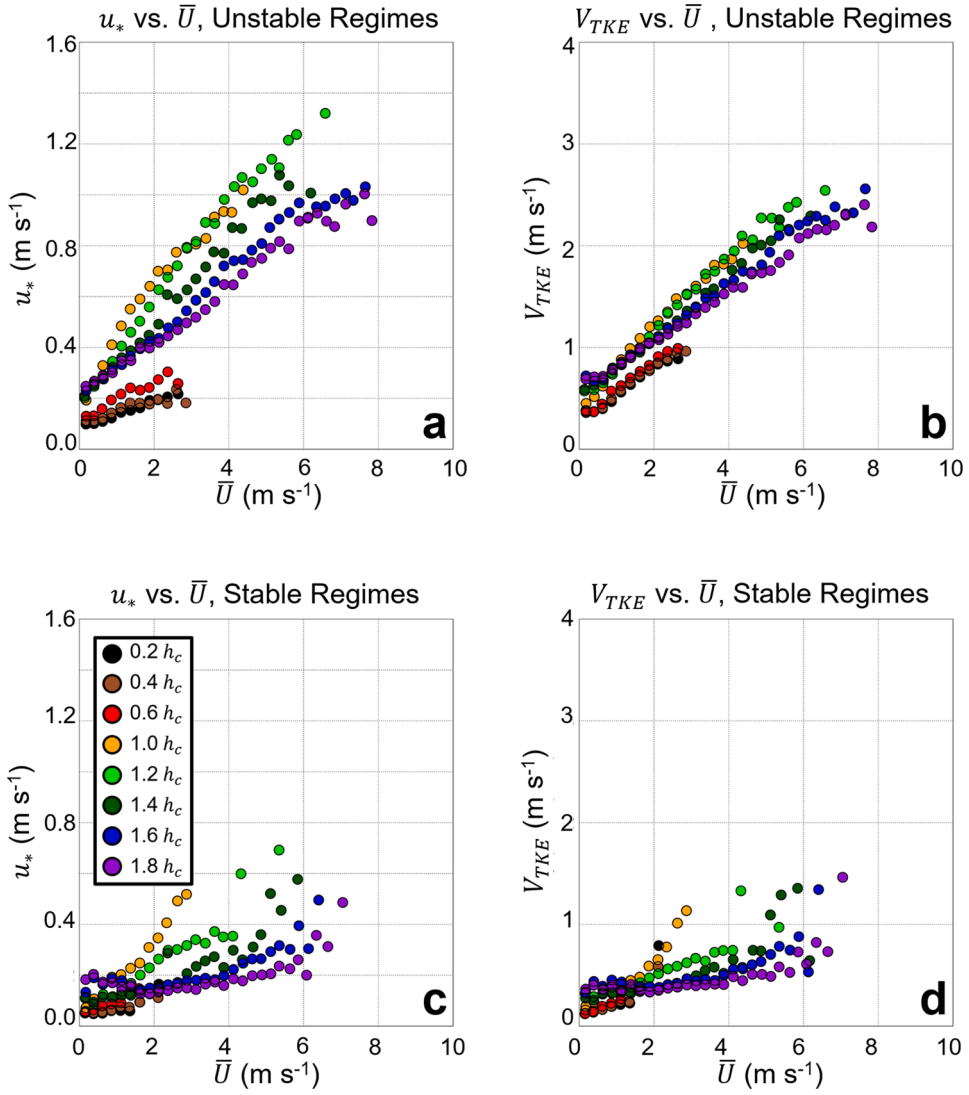

Fig. 15. (a) Mean u_* as a function of $\overline{U}$ for unstable cases (i.e., when $\frac{dT}{dz}$ < 10th percentile). Same for (b) but for V_{TKE}. Same for (c) and (d), respectively, but for stable cases (i.e., when $\frac{dT}{dz}$ > 90th percentile). The colors of the different symbols represent the different heights (see figure legend). A bin size of 0.25 $m\ s^{-1}$ is used in all panels.

(Fig. 11a and b). We also quantified the relationship present in Figs. 10 and 11 by determining the variation of r as a function of height within and above the forest canopy. In January, within-canopy values of r for u_* versus $\overline{U}$ were < 0.5 but exhibited a marked increase above 1.0h_c, with all heights except for 1.8h_c having $r > 0.8$ (Fig. 12a). In July, the relationship was less discernable than in January, as within-canopy values of r were around 0.5 but exhibited larger variability above the canopy than in January. Values of r reached a maximum of about 0.9 directly above the top of the forest canopy and have a marked decrease above the canopy (Fig. 12c).

We observed similar behavior when we quantified the relationship between V_{TKE} and $\overline{U}$ in January and July as we did when we considered the relationship between u_* and $\overline{U}$. Consistent with findings over the entire year, we found that r between V_{TKE} and $\overline{U}$ was larger than r between u_* and $\overline{U}$, and there were marked differences for within-canopy r versus above canopy r, and these were lower in July (Fig. 12d) than in January (Fig. 12b).

Consistent with our findings from Section 4.3, for each $\overline{U}$ bin, both u_* and V_{TKE} were typically largest at h_c than at any other sampling height. This phenomenon was observed during the afternoon and nighttime in both January and July and is indicative of maximum turbulence exchanges at this sampling height resulting in the largest r at this sampling height (cf. Fig. 12).

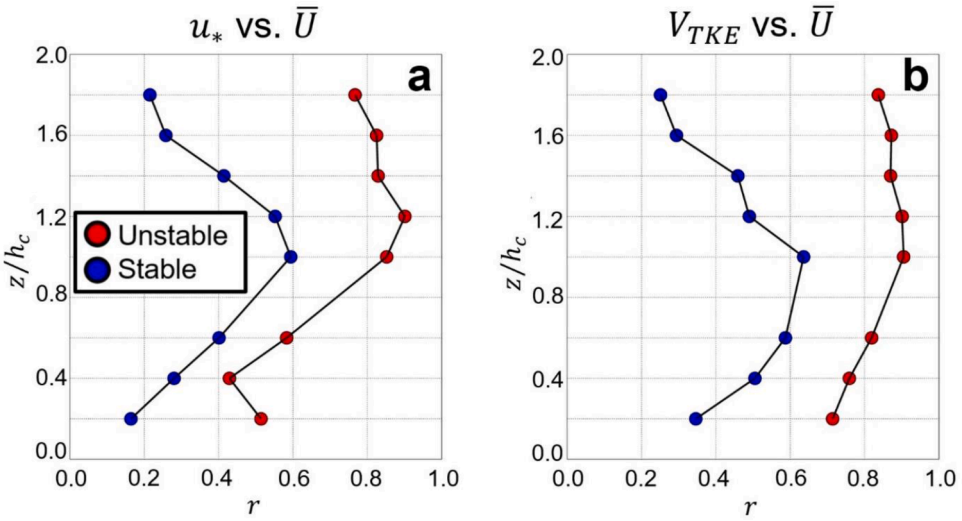

Fig. 16. Pearson correlation coefficient (r) as a function of z/h_c between (a) u_* and $\overline{U}$ and between (b) V_{TKE} and $\overline{U}$ for unstable regimes (i.e., when $\frac{dT}{dz}$ < 10th percentile; red circles) and for stable regimes (i.e., when $\frac{dT}{dz}$ > 90th percentile; blue circles). All values shown are statistically significant at the 0.01 confidence level (i.e., $p < 0.01$),.

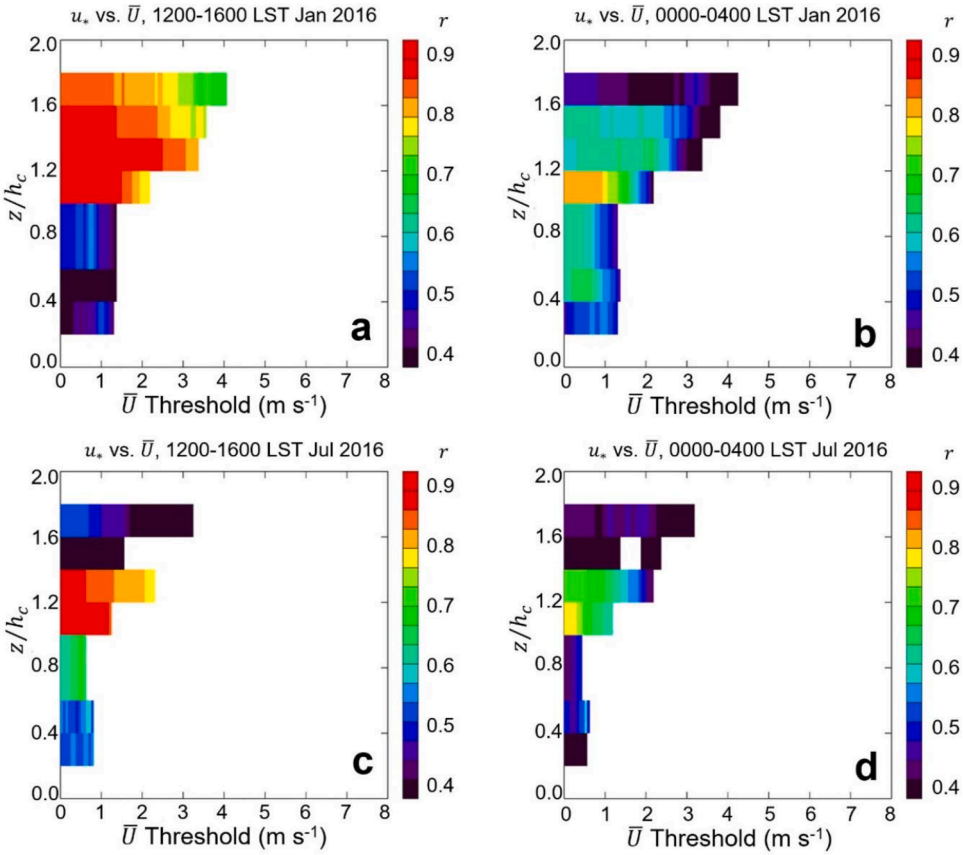

Fig. 17. Pearson correlation coefficient (r) between u_* and $\overline{U}$ as a function of varying $\overline{U}$ thresholds for (a) 1200–1600 LST in January 2016, (b) 0000–0400 LST in January 2016, (c) 1200–1600 LST in July 2016, and (d) 0000–0400 LST in July 2016. Here, the r-values (shading) indicate the relationship between u_* and $\overline{U}$, but only for the subset of cases with $\overline{U}$ above the threshold specified on the x-axis.

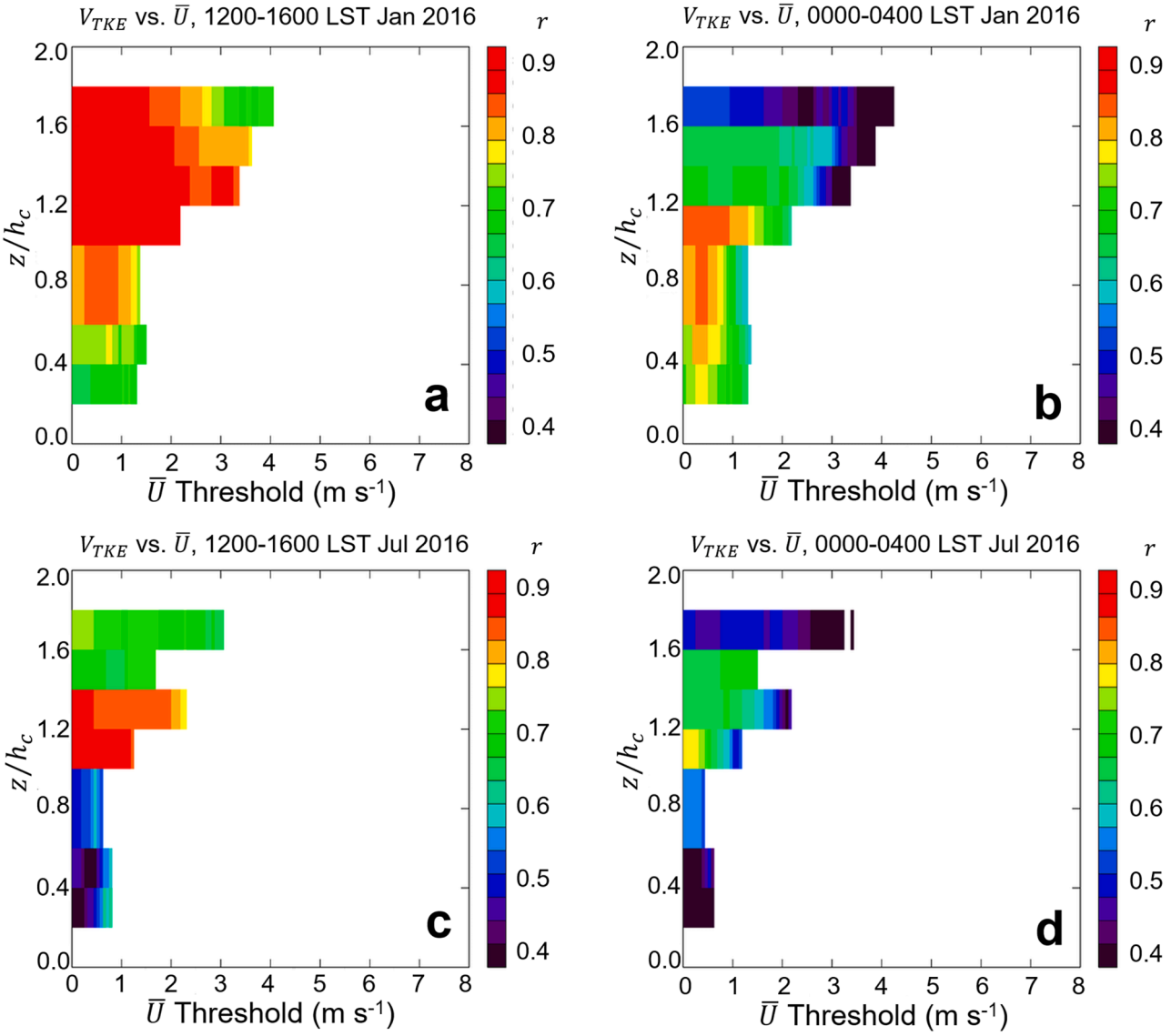

Fig. 18. Same as Fig. 17 but for V_{TKE}.

4.5. Relationship between turbulence and wind speed as a function of wind direction

So far, we have focused on how the relationship between u_* and $\overline{U}$, and between V_{TKE} and $\overline{U}$ vary as a function of time of day and season but have yet to consider how these relationships change with different wind directions. Thus in this section, we evaluate HOST for three different wind direction regimes, i.e. NE winds, SW winds, and NW winds, and conduct this analysis irrespective of time of day and irrespective of season. We found that the relationship between u_* and $\overline{U}$ and between V_{TKE} and $\overline{U}$ showed a similar pattern for the different wind directions (Fig. 13). In general, results indicated that linear dependencies of u_* on both $\overline{U}$ and V_{TKE} became more prominent above a threshold wind speed of about 2 $m\ s^{-1}$ for $h_c < 1$ (i.e., with the canopy), whereas at the uppermost sampling heights (i.e., $1.6h_c$ and $1.8h_c$) the linearity occurred at a threshold wind speed of about 4 $m\ s^{-1}$. For the interim altitudes near h_c (i.e., $1.0h_c$ and $1.2h_c$), there was clear evidence of linearity whereas at $1.4h_c$ there were mixed results with variable wind speed thresholds.

We further quantified the above dependencies by determining the vertical variability of r (as was performed for the aforementioned analyses) and found that NE winds had the largest within-canopy r values, both for u_* versus $\overline{U}$ and V_{TKE} versus $\overline{U}$. Consistent with analyses presented earlier, r was larger for V_{TKE} versus $\overline{U}$ than for u_* versus $\overline{U}$ (Fig. 14). The smallest within-canopy r values occurred for SW and NW winds. Above the canopy, r values were larger than within the canopy, which is also consistent with findings presented earlier in this study. However, we emphasize that the findings on the relationship in V_{TKE} versus $\overline{U}$ and u_* versus $\overline{U}$ were similar for all wind directions, and there was a hockey-stick type relationship present for all wind directions. Furthermore, for a given $\overline{U}$, u_* and V_{TKE} were largest at and immediately above $1.0h_c$ for all wind directions, resulting in an r maximum at $1.0h_c$ and $1.2h_c$ (cf. Fig. 14), suggesting that maximum turbulence exchanges occur at $1.0h_c$ irrespective of wind direction.

4.6. Relationship between turbulence and wind speed as a function of atmospheric stability

To explicitly quantify the impacts of stability on the relationship between turbulence characteristics and wind speed within and above the canopy top as a function of atmospheric stability, we used the observations of $\frac{dT}{dz}$ to distinguish between different two extreme atmospheric stability regimes (i.e., very unstable and very stable) by computing $\frac{dT}{dz}$

percentiles following the approach discussed in Section 3.

Results indicate a larger dependence of both u_* and V_{TKE} on $\overline{U}$ for unstable regimes than for the stable regimes. For instance, we found that, for all sampling heights, the u_* versus $\overline{U}$ slopes were larger for unstable regimes than for stable regimes, and the largest slopes in all instances occurred near h_c (Table 2). We also found that unstable regimes exhibited a linear relationship between both u_* and $\overline{U}$ (Fig. 15a), as well as between V_{TKE} and $\overline{U}$ (Fig. 15b). The relationship between these variables was stronger above the top of the forest canopy, where the value for r between u_* and $\overline{U}$ was around 0.8 ($p < 0.01$, Fig. 16a), and the value for r between V_{TKE} and $\overline{U}$ was around 0.9 ($p < 0.01$, Fig. 16b). We further noted large differences in the relationship between turbulence and wind speed when we consider only stable regimes as compared with unstable regimes. When we considered only stable regimes, we found marked differences between within the canopy and above the forest canopy. Within the canopy, r between u_* and $\overline{U}$ (Fig. 16a) and V_{TKE} and $\overline{U}$ (Fig. 16b) increased with height to around 0.5 and 0.6, respectively, at h_c, whereas above h_c, r decreased. The decrease in r above h_c is due, at least in part, to an inverse relationship between u_* and $\overline{U}$ (cf. Fig 15c) and between V_{TKE} and $\overline{U}$ (cf. Fig. 14d) for low values of $\overline{U}$ (i.e., $< \sim 2\ m\ s^{-1}$).

The findings here suggest the need for alternative parameterizations to MOST, including for example non-local parameterizations or using Richardson-based scaling approaches (e.g., Dyer, 1974; Sorbjan 2010; Sorbjan and Grachev, 2010; Lee and Buban, 2020; Greene et al., 2022) which may better suited for stable conditions (e.g., Sorbjan 2010). Additionally, u_* and V_{TKE} at a given $\overline{U}$ are maximized at the canopy top, with the most apparent differences occurring under stable atmospheric regimes than under unstable regimes (cf. Fig. 15) and resulting in an r maximum at h_c (cf. Fig. 16).

5. Summary, conclusions, and outlook

Overall, our findings were generally consistent with previous studies, as we found a nonlinear relationship between turbulence parameters (i.e., u_* and V_{TKE}) and the mean horizontal wind speed, which was a finding documented in previous work (e.g., Russell et al., 2016; Sun et al., 2020; Bhimireddy et al., 2022). For instance, Russell et al., 2016 used observations from within a mixed coniferous forest in northern Idaho, U.S., and found a linear relationship between σ_w and wind speed during the daytime and under unstable atmospheric regimes. Russell et al., 2016 also observed a non-linear relationship during the nighttime that resembled HOST-type relationships. Bhimireddy et al., 2022, using observations obtained from the Stable Atmospheric Variability and Transport (SAVANT) campaign in central Illinois, U.S., found that the relationship between V_{TKE} and wind speed varied significantly as a function of surface roughness (i.e., preharvest versus postharvest) and as a function of atmospheric stability, with the largest deviations from MOST occurring under weak wind speeds.

Unique to our study, though, is that our work was the first of its kind to use multi-level turbulence measurements to evaluate HOST both within and above a forest canopy. This work further illustrates how the HOST relationships varied by time of day, across contrasting seasons, under changing wind directions, and varying atmospheric stability regimes. Whereas the relationships were fairly similar for different wind directions, atmospheric stability had a much larger influence on these relationships, with large (small) r-values occurring under highly unstable (stable) stability regimes. Furthermore, the largest r-values occurred at the canopy top at the interface between the within-canopy and above-canopy layers. To further corroborate the aforementioned findings, we explored the vertical (i.e., within and above the canopy) and temporal (i.e., afternoon versus nighttime) variability in both turbulence-related correlations (u_* and V_{TKE} across diverse $\overline{U}$ regimes) in January (Fig. 17) and July (Fig. 18). These correlations provide a holistic summary of our findings and underscore the largest r values present at and above the canopy top.

Overall, the relationships between u_* and $\overline{U}$ and between V_{TKE} and $\overline{U}$ were found consistent with each other, indicating that our results are not strongly sensitive to our choice of turbulence parameter. Furthermore, these relationships are typically nonlinear within the forest canopy and are larger during the summer than during the winter. This finding implies turbulence is typically generated by local instabilities rather than being generated via bulk shear (e.g., Sun et al., 2020). Independent of season, however, there is a peak in the correlation at and above the canopy height that is suggestive of maximum turbulence exchanges here. Above the forest canopy, the relationships are more linear during the afternoon than during the nighttime and are stronger during the winter when the canopy is non-foliated than during the summer when the canopy is foliated which is suggestive of turbulence generation through bulk shear under these instances.

Moving forward, it is our intent that the findings from the present study will help to further motivate the need for alternatives to MOST for potential use in SL parameterizations within NWP models, as the present work builds upon many previous studies that have described limitations and weaknesses of MOST by noting scenarios when its performance is insufficient. We anticipate that the implementation of modifications to MOST-derived parameterizations, or even entirely new SL parameterizations, into operational NWP models will help lead to improvements of weather forecasts.

CRediT authorship contribution statement

Temple R. Lee: Writing – review & editing, Writing – original draft, Visualization, Methodology, Investigation, Formal analysis, Conceptualization. **Sandip Pal:** Writing – review & editing, Writing – original draft, Visualization, Methodology, Investigation, Formal analysis. **Praveena Krishnan:** Writing – review & editing, Writing – original draft. **Tim B. Wilson:** Writing – review & editing. **Rick D. Saylor:** Writing – review & editing, Data curation. **Tilden P. Meyers:** Funding acquisition, Data curation, Conceptualization. **John Kochendorfer:** Writing – review & editing, Data curation. **Will Pendergrass:** Resources, Funding acquisition, Data curation, Conceptualization. **Randy White:** Resources, Data curation. **Mark Heuer:** Resources, Data curation.

Declaration of competing interest

The authors declare that they have no known competing financial interests or personal relationships that could have appeared to influence the work reported in this paper.

Data availability

The turbulent fluxes and meteorological measurements used in this study are available upon request from the corresponding author. The digital elevation model used in Fig. 1 was obtained from the Parameter-elevation Regressions on Independent Slopes Model (PRISM) climate group at the Northwest Alliance for Computational Science and Engineering and can be accessed from <https://prism.oregonstate.edu/downloads/>.

Acknowledgments

We thank the engineers and technicians from the NOAA Air Resources Laboratory Atmospheric Turbulence and Diffusion Division in Oak Ridge, Tennessee who have helped to maintain the instrumentation at Chestnut Ridge to ensure high-quality datasets from the site. Co-author Sandip Pal was supported via internal funding from the Department of Geosciences at Texas Tech University. Additionally, we thank Ms. Gretchen Lee of the Scylla Group in Winchester, Virginia for her

assistance with Fig. 2. Furthermore, we gratefully acknowledge the feedback and suggestions from the two anonymous reviewers which helped us improve the scientific content of this manuscript. Finally, we note that the results and conclusions obtained from this work, as well as any views that we expressed herein, are those of the authors and may not necessarily reflect the views of NOAA or the Department of Commerce.

References

Acevedo, O.C., Mahrt, L., Puhales, F.S., Costa, F.D., Medeiros, L.E., Degrazia, G.A., 2016. Contrasting structures between the decoupled and coupled state of the stable boundary layer. Q. J. Roy. Meteor. Soc. 142, 693–702. https://doi.org/10.1002/qj.2693.

Allouche, M., Bou-Zeid, E., Ansorge, C., Katul, G.G., Chamecki, M., Acevedo, O., Thanekar, S., Fuentes, J.D., 2022. The detection, genesis, and modeling of turbulence intermittency in the stable atmospheric surface layer. J. Atmos. Sci. 79, 1171–1190. https://doi.org/10.1175/JAS-D-21-0053.1.

Anand, M., Pal, S., 2023. Exploring atmospheric boundary layer depth variability in frontal environments over an arid region. Boundary-Layer Meteorol 186, 251–285. https://doi.org/10.1007/s10546-022-00756-z.

Andreas, E.L., Hicks, B.B., 2002. Comments on "Critical test of the validity of Monin–Obukhov similarity during convective conditions. J. Atmos. Sci. 59, 2605–2607. https://doi.org/10.1175/1520-0469(2002)059<2605:COCTOT>2.0.CO;2.

Andreas, E.L., Mahrt, L., Vickers, D., 2012. A new drag relation for aerodynamically rough flow over the ocean. J. Atmos. Sci. 69, 2520–2537. https://doi.org/10.1175/JAS-D-11-0312.1.

Ansorge, C., Mellado, J.P., 2014. Global intermittency and collapsing turbulence in the stratified planetary boundary layer. Bound.-Layer Meteorol 153, 89–116. https://doi.org/10.1007/s10546-014-9941-3.

Ansorge, C., Mellado, J.P., 2016. Analyses of external and global intermittency in the logarithmic layer of Ekman flow. J. Fluid. Mech. 805, 611–635. https://doi.org/10.1017/jfm.2016.534.

Bhimireddy, S.R., Wang, J., Hiscox, A.L., Kristovich, D.A.R., 2022. Influence of stability and surface roughness on turbulence during the Stable Atmospheric Variability and Transport (SAVANT) field campaign. J. Appl. Meteor. Climatol. 61, 1273–1289. https://doi.org/10.1175/JAMC-D-21-0160.1.

Bhimireddy, S.R., Sun, J., Wang, J., Kristovich, D.A., Hiscox, A.L., 2024. Effect of small-scale topographical variations and fetch from roughness elements on the stable boundary layer turbulence statistics. Bound. -Lay. Meteorol 190, 3. https://doi.org/10.1007/s10546-023-00855-5.

Brunet, Y., 2020. Turbulent flow in plant canopies: historical perspective and overview. Bound.-Lay. Meteorol 177, 315–364. https://doi.org/10.1007/s10546-020-00560-7.

Businger, J.A., Wyngaard, J.C., Izumi, Y., Bradley, E.F., 1971. Flux-profile relationships in the atmospheric surface layer. J. Atmos. Sci. 28, 181–189. https://doi.org/10.1175/1520-0469(1971)028<0181:FPRITA>2.0.CO;2.

Chechin, D., 2021. On the u⋆− U relationship in the stable atmospheric boundary layer over Arctic sea ice. Atmosphere (Basel) 12, 591. https://doi.org/10.3390/atmos12050591.

Dyer, A.J., 1974. A review of flux-profile relationships. Bound.-Layer Meteor 7, 363–372. https://doi.org/10.1007/BF00240838.

Fernando, H.J.S., Pardyjak, E.R., Di Sabatino, S., Chow, F.K., De Wekker, S.F.J., Hoch, S. W., Hacker, J., Pace, J.C., Pratt, T., Pu, Z., Steenburgh, W.J., Whiteman, C.D., Wang, Y., Zajic, D., Balsley, B., Dimitrova, R., Emmitt, G.D., Higgins, C.W., Hunt, J. C.R., Knievel, J.C., Lawrence, D., Liu, Y., Nadeau, D.F., Kit, E., Blomquist, B.W., Conry, P., Coppersmith, R.S., Creegan, E., Felton, M., Grachev, A., Gunawardena, N., Hang, C., Hocut, C.M., Huynh, G., Jeglum, M.E., Jensen, D., Kulandaivelu, V., Lehner, M., Leo, L.S., Liberzon, D., Massey, J.D., McEnerney, K., Pal, S., Price, T., Sghiatti, M., Silver, Z., Thompson, M., Zhang, H., Zsedrovits, T., 2015. The MATERHORN: unraveling the intricacies of mountain weather. Bull. Amer. Meteor. Soc. 96, 1945–1967. https://doi.org/10.1175/BAMS-D-13-00131.1.

Foken, T., 2006. 50 years of the Monin–Obukhov similarity theory. Bound.-Layer Meteor 119, 431–447. https://doi.org/10.1007/s10546-006-9048-6.

Greco, S., Baldocchi, D.D., 1996. Seasonal variations of CO2 and water vapour exchange rates over a temperate deciduous forest. Global Change Biol 2, 183–197. https://doi.org/10.1111/j.1365-2486.1996.tb00071.x.

Greene, B.R., Kral, S.T., Chilson, P.B., Reuder, J., 2022. Gradient-based turbulence estimates from multicopter profiles in the Arctic stable boundary layer. Bound.-Layer Meteor 183, 321–353. https://doi.org/10.1007/s10546-022-00693-x.

Grisogono, B., Sun, J., Belušić, D., 2020. A note on MOST and HOST for turbulence parametrization. Q. J. Roy. Meteor. Soc. 146, 1991–1997. https://doi.org/10.1002/qj.3770.

Hanson, P.J., Wullschleger, S.D., 2003. Ecological Studies: North American Temperature Deciduous Forest Responses to Changing Precipitation Regimes, 166. Springer, New York.

Hicks, B.B., 1978. Some limitations of dimensional analysis and power laws. Bound.-Layer Meteor 14, 567–569. https://doi.org/10.1007/BF00121895.

Hicks, B.B., 1981. An examination of turbulence statistics in the surface boundary layer. Bound.-Layer Meteor 21, 389–402. https://doi.org/10.1007/BF00119281.

Klink, K., 1999. Climatological mean and interannual variance of United States surface wind speed, direction and velocity. Int. J. Climatol. 19, 471–488. https://doi.org/10.1002/(SICI)1097-0088(199904)19:5<471::AID-JOC367>3.0.CO;2-X.

Lee, T.R., De Wekker, S.F.J., Andrews, A.E., Kofler, J., Williams, J., 2012. Carbon dioxide variability during cold front passages and fair weather days at a forested mountaintop site. Atmos. Environ. 46, 405–416. https://doi.org/10.1016/j.atmosenv.2011.09.06.

Lee, T.R., De Wekker, S.F.J., Pal, S., Andrews, A.E., Kofler, J., 2015. Meteorological controls on the diurnal variability of carbon monoxide mixing ratio at a mountaintop monitoring site in the Appalachian Mountains. Tellus B 67, 25659. https://doi.org/10.3402/tellusb.v67.25659.

Lee, T.R., Buban, M., Turner, D.D., Meyers, T.P., Baker, C.B., 2019. Evaluation of the High-Resolution Rapid Refresh (HRRR) model using near-surface meteorological and flux observations from Northern Alabama. Wea. Forecast. 34, 635–663. https://doi.org/10.1175/WAF-D-18-0184.1.

Lee, T.R., Buban, M., 2020. Evaluation of Monin-Obukhov and bulk Richardson parameterizations for surface-atmosphere exchange. J. Appl. Meteor. Climatol. 59, 1091–1107. https://doi.org/10.1175/JAMC-D-19-0057.1.

Lee, T.R., Buban, M.S., Meyers, T.P., 2021. Application of bulk Richardson parameterizations of surface fluxes to heterogeneous land surfaces. Mon. Weather Rev. 149, 3243–3264. https://doi.org/10.1175/MWR-D-21-0047.1.

Lee, T.R., Meyers, T.P., 2023. New parameterizations of turbulence statistics for the atmospheric surface layer. Mon. Weather Rev. 151, 85–103. https://doi.org/10.1175/MWR-D-22-0071.1.

Lee, T.R., Leeper, R.D., Wilson, T., Diamond, H., Meyers, T.P., Turner, D.D., 2023a. Identifying biases in near- and sub-surface meteorological fields in the High-Resolution Rapid Refresh (HRRR) weather prediction model. Wea. Forecast. 38, 879–900. https://doi.org/10.1175/WAF-D-22-0213.1.

Lee, T.R., Pal, S., Krishnan, P., Hirth, B., Heuer, M., Meyers, T.P., Saylor, R.D., Schroeder, J., 2023b. On the efficacy of Monin-Obukhov and bulk Richardson surface-layer parameterizations over drylands. J. Appl. Meteor. Climatol 62, 855–875. https://doi.org/10.1175/JAMC-D-23-0092.1.

Lee, T.R., Pal, S., Leeper, R.D., Wilson, T., Diamond, H., Meyers, T.P., Turner, D.D., 2024. On the importance of regime-specific evaluations for numerical weather prediction models as demonstrated using the High Resolution Rapid Refresh (HRRR) model. Wea. Forecast. 39, 781–791. https://doi.org/10.1175/WAF-D-23-0177.1.

Liang, X., Miao, S., Li, J., Bornstein, R., Zhang, X., Gao, Y., Chen, F., Cao, X., Cheng, Z., Clements, C., Dabberdt, W., 2018. SURF: understanding and predicting urban convection and haze. Bull. Am. Meteorol. Soc. 99, 1391–1413. https://doi.org/10.1175/BAMS-D-16-0178.1.

Mahrt, L., 1998. Stratified atmospheric boundary layers and breakdown of models. Theor. Comput. Fluid Dyn. 11, 263–279. https://doi.org/10.1007/s001620050093.

McCaffrey, K., Quelet, P.T., Choukulkar, A., Wilczak, J.M., Wolfe, D.E., Oncley, S.P., Brewer, W.A., Debnath, M., Ashton, R., Iungo, G.V., Lundquist, J.K., 2017. Identification of tower-wake distortions using sonic anemometer and lidar measurements. Atmos. Meas. Tech. 10, 393–407. https://doi.org/10.5194/amt-10-393-2017.

Meyers, T.P., 2001. A comparison of summertime water and CO2 fluxes over rangeland for well watered and drought conditions. Agric. For. Meteor. 106, 205–214. https://doi.org/10.1016/S0168-1923(00)00213-6.

Meyers, T.P., 2016. AmeriFlux BASE US-ChR Chestnut Ridge, Ver. 2-1, AmeriFlux AMP, accessed 24 November 2023.

Mohan, M., Siddiqui, T.A., 1998. Analysis of various schemes for the estimation of atmospheric stability classification. Atmos. Environ. 32, 3775–3781. https://doi.org/10.1016/S1352-2310(98)00109-5.

Monin, A.S., Obukhov, A.M., 1954. Basic laws of turbulent mixing in the surface layer of the atmosphere. Tr. Geofiz. Inst., Akad. Nauk SSSR 24, 163–187.

Optis, M., Monahan, A., Bosveld, F.C., 2014. Moving beyond Monin–Obukhov similarity theory in modelling wind-speed profiles in the lower atmospheric boundary layer under stable stratification. Bound.-Layer Meteor 153, 497–514. https://doi.org/10.1007/s10546-014-9953-z.

Pal, S., Lee, T.R., Phelps, S., De Wekker, S.F.J., 2014. Impact of atmospheric boundary layer depth variability and wind reversal on the diurnal variability of aerosol concentration at a valley site. Sci. Total Environ. 496, 424–434. https://doi.org/10.1016/j.scitotenv.2014.07.067.

Pal, S., Lee, T.R., De Wekker, S.F.J., 2017. A study of the combined impact of boundary layer height and near-surface meteorology on the CO diurnal cycle at a low mountaintop site using simultaneous lidar and in-situ observations. Atmos. Environ. 164, 165–179. https://doi.org/10.1016/j.atmosenv.2017.05.041.

Pal, S., Lee, T.R., 2019. Advected air mass reservoirs in the downwind of mountains and their roles in overrunning boundary layer depths over the plains. Geophys. Res. Lett. 46, 10140–10149. https://doi.org/10.1029/2019GL083988.

Pal, S., Haeffelin, M., Batchvarova, E., 2013. Exploring a geophysical process-based attribution technique for the determination of the atmospheric boundary layer depth using aerosol lidar and near-surface meteorological measurements. J. Geophys. Res. Atmos. 118, 9277–9295. https://doi.org/10.1002/jgrd.50710.

Peltola, O., Lapo, K., Thomas, C.K., 2021. A physics-based universal indicator for vertical decoupling and mixing across canopies architectures and dynamic stabilities. Geophys. Res. Lett. 48. https://doi.org/10.1029/2020GL091615. e2020GL091615.

Poulos, G.S., Blumen, W., Fritts, D.C., Lundquist, J.K., Sun, J., Burns, S.P., Nappo, C., Banta, R., Newsom, R., Cuxart, J., Terradellas, E., Balsley, B., Jensen, M., 2002. CASES-99: a comprehensive investigation of the stable nocturnal boundary layer. Bull. Amer. Meteor. Soc. 83, 555–582. https://doi.org/10.1175/1520-0477(2002)083<0555:CACIOT>2.3.CO;2.

Rigden, A., Li, D., Salvucci, G., 2018. Dependence of thermal roughness length on friction velocity across land cover types: a synthesis analysis using AmeriFlux data. Agric. For. Meteor. 249, 512–519. https://doi.org/10.1016/j.agrformet.2017.06.003.

Russell, E.S., Liu, H., Gao, Z., Lamb, B., Wagenbrenner, N., 2016. Turbulence dependence on winds and stability in a weak-wind canopy sublayer over complex terrain.

J. Geophys. Res. Atmos. 121, 11502–11515. https://doi.org/10.1002/2016JD025057.
Salesky, S.T., Chamecki, M., 2012. Random errors in turbulence measurements in the atmospheric surface layer: implications for Monin–Obukhov similarity theory. J. Atmos. Sci. 69, 3700–3714. https://doi.org/10.1175/JAS-D-12-096.1.
Sedefian, L., Bennet, E., 1980. A comparison of turbulence classification schemes. Atmos. Environ. 14, 741–750. https://doi.org/10.1016/0004-6981(80)90128-.
Sfyri, E., Rotach, M.W., Stiperski, I., Bosveld, F.C., Lehner, M., Obleitner, F., 2018. Scalar-flux similarity in the layer near the surface over mountainous terrain. Bound.-Layer Meteor 169, 11–46. https://doi.org/10.1007/s10546-018-0365-3.
Sorbjan, Z., 2010. Gradient-based scales and similarity laws in the stable boundary layer. Q. J. Royal Meteor. Soc. 136, 1243–1254. https://doi.org/10.1002/qj.638.
Sorbjan, Z., Grachev, A.A., 2010. An evaluation of the flux–gradient relationship in the stable boundary layer. Bound.-Layer Meteor 135, 385–405. https://doi.org/10.1007/s10546-010-9482-3.
Sun, J., Mahrt, L., Banta, R.M., Pichugina, Y.L., 2012. Turbulence regimes and turbulence intermittency in the stable boundary layer during CASES-99. J. Atmos. Sci. 69, 338–351. https://doi.org/10.1175/JAS-D-11-082.1.
Sun, J., Mahrt, L., Nappo, C., Lenschow, D.H., 2015. Wind and temperature oscillations generated by wave–turbulence interactions in the stably stratified boundary layer. J. Atmos. Sci. 72, 1484–1503. https://doi.org/10.1175/JAS-D-14-0129.1.
Sun, J., Lenschow, D.H., LeMone, M.A., Mahrt, L., 2016. The role of large-coherent-eddy transport in the atmospheric surface layer based on CASES-99 observations. Bound.-Layer Meteor 160, 83–111. https://doi.org/10.1007/s10546-016-0134-0.
Sun, J., Takle, E.S., Acevedo, O.C., 2020. Understanding physical processes represented by the Monin-Obukhov bulk formula for momentum transfer. Bound.-Layer Meteor 177, 69–95. https://doi.org/10.1007/s10546-020-00546-5.
Van de Wiel, B.J.H., Moene, A.F., Jonker, H.J.J., Baas, P., Basu, S., Donda, J.M.M., Sun, J., Holtslag, A.A.M., 2012. The minimum wind speed for sustainable turbulence in the nocturnal boundary layer. J. Atmos. Sci. 69, 3116–3127. https://doi.org/10.1175/JAS-D-12-0107.1.
Meyers, T.P., Baldocchi, D.D., 2005. Current micrometeorological flux methodologies with applications in agriculture. Micrometeorology in Agricultural Systems. Agronomy Monogr 47, 381–396. American Society of Agronomy, Crop Science Society of America, and Soil Science Society of America. https://doi.org/10.2134/agronmonogr47.c16.
Vignon, E., van de Wiel, B.J.H., van Hooijdonk, I.G.S., Genthon, C., van der Linden, S.J.A., van Hooft, J.A., Baas, P., Maurel, W., Traullé, Casasanta G., 2017. Stable boundary-layer regimes at Dome C, Antarctica: observation and analysis. Q. J. Roy. Meteor. Soc. 143, 1241–1253. https://doi.org/10.1002/qj.2998.
Wilson, K.B., Baldocchi, D.D., 2000. Seasonal and interannual variability of energy fluxes over a broadleaved temperate deciduous forest in North America. Agric. For. Meteor. 100, 1–18. https://doi.org/10.1016/S0168-1923(99)00088-X.
Wilson, K.B., Hanson, P.J., Baldocchi, D.D., 2000. Factors controlling evaporation and energy partitioning beneath a deciduous forest over an annual cycle. Agric. For. Meteor. 102, 83–103. https://doi.org/10.1016/S0168-1923(00)00124-6.
Wilson, K.B., Baldocchi, D.D., Aubinet, M., Berbigier, P., Bernhofer, C., Dolman, H., Falge, E., Field, C., Goldstein, A., Granier, A., Grelle, A., Halldor, T., Hollinger, D., Katul, G., Law, B.E., Lindroth, A., Meyers, T., Moncrieff, J., Monson, R., Oechel, W., Tenhunen, J., Valentini, R., Verma, S., Vesala, T., Wofsy, S., 2002. Energy partitioning between latent and sensible heat flux during the warm season at FLUXNET sites. Water Resour. Res. 38, 30–31. https://doi.org/10.1029/2001WR000989.
Wilson, T.B., Meyers, T.P., 2007. Determining vegetation indices from solar and photosynthetically active radiation fluxes. Agric. For. Meteor. 144, 160–179. https://doi.org/10.1016/j.agrformet.2007.04.001.
Wilson, J.D., 2008. Monin-Obukhov functions for standard deviations of velocity. Bound.-Layer Meteor 129, 353–369. https://doi.org/10.1007/s10546-008-9319-5.
Wilson, T.B., Meyers, T.P., Kochendorfer, J., Anderson, M.C., Heuer, M., 2012. The effect of soil surface litter residue on energy and carbon fluxes in a deciduous forest. Agric. For. Meteor. 61, 134–147. https://doi.org/10.1016/j.agrformet.2012.03.013.
Wulfmeyer, V., Behrendt, A., Kottmeier, C., Corsmeier, U., Barthlott, C., Craig, G.C., et al., 2011. The convective and Orographically-induced precipitation study (COPS): the scientific strategy, the field phase, and research highlights. Q. J. Roy. Meteor. Soc. 137, 3–30. https://doi.org/10.1002/qj.752.
Yi, C., Davis, K.J., Berger, B.W., Bakwin, P.S., 2001. Long-term observations of the dynamics of the continental planetary boundary layer. J. Atmos. Sci. 58, 1288–1299.
Yus-Díez, J., Udina, M., Soler, M.R., Lothon, M., Nilsson, E., Bech, J., Sun, J., 2019. Nocturnal boundary layer turbulence regimes analysis during the BLLAST campaign. Atmos. Chem. Phys. 19, 9495–9514. https://doi.org/10.5194/acp-19-9495-2019.
Zhang, D.-L., Zheng, W.-Z., 2004. Diurnal cycles of surface winds and temperatures as simulated by five boundary layer parameterizations. J. Appl. Meteor. Climatol. 43, 157–169. https://doi.org/10.1175/1520-0450(2004)043<0157:DCOSWA>2.0.CO;2.